Pulsing inertial oscillation, supercell storms, and surface mesonetwork data

R. C. COSTEN[1] and L. J. MILLER[2]

[1]*NASA Langley Research Center, Hampton, Virginia 23681-2199 USA*

[2]*National Center for Atmospheric Research,* Boulder, Colorado 80307-3000 USA*

Abstract. The pulsing inertial oscillation (PIO) model is a nonlinear, time-dependent, translating vortex solution of the inviscid, compressible fluid dynamic equations in the middle troposphere. The translation of this vortex during a pulse is strikingly similar to that of a supercell storm -- a rotating thunderstorm that can generate tornadoes and hail. Two studies were performed to test the hypothesis that some supercell storms are manifestations of a PIO pulse. The first study applied the model to an intense interior draft whose buoyancy was bounded by a temperature excess of ± 12 K. The peak updraft speed achieved was 41.5 m s^{-1} and the peak Rossby number was 92.9. The study also pointed to an advanced concept for attaining higher values. The second study applied the PIO model to a supercell storm as a whole and succeeded in replicating its bulk properties, such as mesocyclonic circulation, net mass and moisture influxes, and time track. This study also identified a critical feature of the PIO model that could be tested against storm data: The average vertical draft is downward before the turn in the storm track and upward afterwards. In the conventional theory, the average vertical draft is upward from storm inception until dissipation. These differing draft predictions were compared with the best available data, which are surface mesonetwork data. These data were found to support the PIO model. However, surface data alone are not conclusive, and further measurements are warranted.

---

* The National Center for Atmospheric Research is sponsored by the National Science Foundation.

Key Words: Modeling, supercell storm, nonlinear, inertial oscillation, mesonetwork data.

1. Introduction

A supercell storm is a rotating thunderstorm that can generate tornadoes and hail. A salient feature of supercell storms is that, upon spin-up, the track of a cyclonic supercell turns to the right and that of an anticyclonic supercell turns to the left (Fujita and Grandoso [1]). We present a novel solution for a tropospheric vortex that has the same feature. The model is nonlinear and is called the pulsing inertial oscillation (PIO). Two studies are made to test the hypothesis that some supercell storms are manifestations of a PIO pulse.

These studies revive Ferrel's [2] concept that the rotation of a supercell storm is caused by the Coriolis force. This concept has remained dormant for many years, partly because of scaling studies by Wallace and Hobbs [3], Morton [4], Holton [5, pp. 1-19], Davies-Jones [6], and others that concluded that the Coriolis force is too weak to spin up a supercell storm in the observed time. The PIO model is a counterexample that negates this conclusion.

The source of rotation in the conventional theory, as reviewed by Bengtsson and Lighthill [7], Kessler [8], Ray [9], Klemp [10], Church *et al.* [11], and others, is horizontal vorticity associated with vertical wind shear. An initial buoyant updraft tilts and stretches the horizontal vortex lines and forms two counter-rotating storms that split apart, as shown numerically by Schlesinger [12]. Although such storm splitting has been observed on radar by Fujita and Grandoso [1], Brown [13], and others, it occurs infrequently compared with cyclonic supercells, according to Davies-Jones [6]. This apparent difficulty with the conventional model was resolved as follows: Maddox [14] showed that the vertical windshear vector in the lower troposphere usually turns clockwise with increasing height in the vicinity of a supercell storm. Using numerical simulations, Klemp and Wilhelmson [15] then showed that this turning vector strengthens the cyclonic storm and weakens the anticyclonic storm. If the weakened storm should produce little precipitation, it would be invisible to radar.

Although the conventional model is highly developed and successful in certain respects, some fundamental questions remain unanswered. For example, as mentioned by Lilly [16] and

Klemp [10], the model does not explain the rightward translation of a cyclonic supercell. Also, the conventional model misplaces the initial development of a tornadic vortex – a vortex of Rossby number about 1000 that precedes a tornado by about 20 min. According to the conventional model, a tornadic vortex originates at the surface, while Doppler radar indicates that it originates at midheight in a supercell [6,11,17].

The PIO model consists of a partly analytic, partly numerical solution of the inviscid, compressible fluid dynamic equations for a translating vortex in the middle troposphere. Compatible solutions are assumed for the boundary and upper layers. The core radius of the PIO model is arbitrary below about 60 km, so the model can be applied to a supercell storm as a whole or to an intense internal draft. The latter is the subject of our first study, which is aimed at determining the upper limits to updraft speed and vorticity relative to the production of hail and a tornadic vortex.

The second study treats the storm as a whole. In its present rudimentary form, the PIO model does not resolve coexisting updrafts and downdrafts, but instead treats the time-dependent *spatial average* vertical draft. This average vertical draft is found to be *negative* during spin-up -- in contrast to the conventional model, where it is positive during spin-up. We compare these differing model predictions with the best available data, which are found to be surface mesonetwork data.

Costen and Stock [18] applied the PIO model to a supercell hailstorm that occurred during the National Hail Research Experiment (NHRE) in northeast Colorado, USA, on 22 July 1972. (We will refer to this supercell, which is documented by Foote and Fankhauser [19], as the *Colorado* hailstorm.) The mesocyclone was already spun up before this storm entered the NHRE mesonetwork, so no analysis of surface data was done.

In the second study, we apply the PIO model to a supercell hailstorm that originated *inside* the mesonetwork of the Cooperative Convective Precipitation Experiment (CCOPE) in southeast Montana, USA, at 0030 UTC on 12 July 1981. (We will refer to this storm, which is documented by Fankhauser *et al.* [20], as the *Montana* hailstorm.) The CCOPE mesonetwork is

described by Knight [21] and the data quality by Wade [22]. After originating within the mesonetwork, this storm developed into a cyclonic supercell that produced baseball- to grapefruit-size hail, and its track turned to the right while still on the mesonetwork. Therefore, this data set is appropriate for testing the PIO and conventional models.

2. PIO model

2.1. TANGENTIAL COORDINATE FRAME

The coordinate frame is a local tangential Cartesian frame where the origin is fixed at mean sea level (MSL) and the x–, y–, and z – axes point eastward, northward, and upward, respectively. (Cylindrical coordinates $r, \theta,$ and z are also used, where $x = r\cos\theta$ and $y = r\sin\theta$.) Although the $x-$ and $y-$ axes do not curve with the surface, this frame is adequate for describing tropospheric flows within a horizontal radius of about 60 km [23, pp. 164-166]. This radius is sufficient to contain the convective core of a supercell, but not all the outer flow.

In the Cartesian frame, the fluid velocity is denoted by $\mathbf{v} = (u, v, w)$ (in m s^{-1}), the vorticity by $\omega = \text{curl } \mathbf{v} = (\xi, \eta, \zeta)$ (in s^{-1}), the divergence by $D = \text{div } \mathbf{v}$ $= (\partial u/\partial x + \partial v/\partial y + \partial w/\partial z)$ (in s^{-1}), and the angular velocity of the Earth by $\Omega = (0, \Omega_y, \Omega_z)$ (in rad s^{-1}). The components Ω_y and Ω_z, although slowly varying functions of y, are treated as constants.

2.2. STORM IDEALIZATIONS AND ZEROTH-ORDER APPROXIMATION

Miller *et al.* [24] present Doppler radar measurements of a supercell storm that show a boundary layer near the surface, a highly sheared layer near the top, an updraft that has its maximum at midheight, two downdrafts, and a mesocyclone. As mentioned, the cylinder shown in Figure 1 is intended to represent, in highly simplified form, either the entire convective core of a supercell or an intense internal draft. Our analysis is confined to the midtropospheric layer $(b \le z \le h)$, which excludes the boundary and upper layers wherein compatible flows are assumed. Lateral entrainment, friction, heat conduction, and radiation are neglected.

As shown in Figure 1, the PIO model is a rotating and dilatating vertical draft of radius $a(t)$. The centerline is located at $(x_c(t), y_c(t))$. The mesocyclone is represented by a Rankine

vortex of vorticity $\zeta(t)$, which is uniform inside the core $(r \le a(t))$ and zero in the outer region $(r \ge a(t))$. To emphasize compressibility, the density ρ (in kg m^{-3}) is taken to decrease exponentially with height z, which also implies that the temperature lapse is zero between b and h. For our purposes, this isothermal approximation is preferable to the constant density approximation used in the supercell studies by Rotunno and Klemp [25] and Lilly [26]. Rising parcels of air expand with divergence $D(t)$, which is also uniform inside the core and zero in the outer region. The core fluid is uniformly buoyant with a normalized density deficit $B(t)$, which is called simply the buoyancy. The fields $\omega(t), D(t)$, and $B(t)$ are zeroth-order approximations to the instantaneous *spatial average* vorticity, divergence, and buoyancy in the core. This property will be used when the model is compared with storm data.

The density of the outer fluid at radius a is given by

$$\rho^0(a,z) = \rho_b{}^0 e^{-\varepsilon Z} \tag{1a}$$

where the fields in the outer region are distinguished by the superscript 0 and $Z \equiv z - b$. The coefficient $\rho_b{}^0$ and the inverse density scale height ε (in m^{-1}) are constants. Inside the core, the density is given by

$$\rho(z,t) = \rho_b{}^0 [1 - B(t)] e^{-\varepsilon Z} \tag{1b}$$

The buoyancy $B(t) << 1$, because it corresponds to a temperature excess or deficit of at most about 12 K [24] and terms of $O(B^2)$ will always be neglected.

The continuity equation is given by

$$\frac{\partial \rho}{\partial t} + \mathbf{v} \cdot \nabla \rho + \rho D = 0 \tag{2}$$

Substituting the inner density (1b) in (2) and retaining the effects of $B(t)$ on the buoyant force but neglecting its effects on $D(t)$, in accordance with one of the Boussinesq approximations [27], we have

$$D(t) = \varepsilon\, w(t) \tag{3a}$$

It follows that the vertical component of velocity $w(t)$ is also spatially uniform inside the core and that $D(t)$ is purely horizontal divergence given by

$$D(t) = \frac{\partial u}{\partial x} + \frac{\partial v}{\partial y} \tag{3b}$$

Equation (3a) is a key approximation of this study and $w(t)$ and $D(t)/\varepsilon$ will be used interchangeably. Also included in the core is a horizontal flow with vertical windshear that is represented by the constants U_b and V_b and the horizontal vorticity components $\xi(t)$ and $\eta(t)$.

3. Inner reduction

3.1. VELOCITY FIELD

The complete velocity field inside the core is given by

$$u(x,y,z,t) = U_b + \eta(t)Z + \frac{1}{2}[D(t)X(x,t) - \zeta(t)Y(y,t)] \tag{4a}$$

$$v(x,y,z,t) = V_b - \xi(t)Z + \frac{1}{2}[D(t)Y(y,t) + \zeta(t)X(x,t)] \tag{4b}$$

$$w(x,y,z,t) = w(t) = \frac{D(t)}{\varepsilon} \tag{4c}$$

where $X(x,t) \equiv x - x_c(t)$ and $Y(y,t) \equiv y - y_c(t)$. The constants U_b and V_b represent the stationary part of the horizontal flow *inside* the core, and $\eta(t)Z$ and $-\xi(t)Z$ represent the *inner* vertical windshear. The terms $-\zeta(t)Y/2$ and $\zeta(t)X/2$ represent the inner flow of the Rankine vortex. The angular velocity of the core fluid $\dot{\theta}$ (in rad s^{-1}) is given by

$$\dot{\theta} = \frac{\zeta}{2} \tag{5}$$

where an overhead dot denotes an ordinary time derivative. The terms $D(t)X/2$ and $D(t)Y/2$ represent the inner radial horizontal flow that results from the divergence.

3.2. MOMENTUM EQUATION

The inviscid momentum equation is given by

$$\frac{\partial \mathbf{v}}{\partial t} + \omega \times \mathbf{v} + \nabla \frac{v^2}{2} + \frac{\nabla p}{\rho} + \nabla \Phi + 2\Omega \times \mathbf{v} = 0 \tag{6}$$

where v^2 is $\mathbf{v} \cdot \mathbf{v}$, p is the pressure (Pa), Φ is the geopotential, gz ($m^2\ s^{-2}$), g is the gravitational acceleration (9.81 $m\ s^{-2}$).

Solving (6) for ∇p and substituting the inner velocity field (4) we find

$$\frac{\partial p}{\partial x} = -\frac{\rho}{2}\left(G_1 - G_3 v + Du\right) \tag{7a}$$

$$\frac{\partial p}{\partial y} = -\frac{\rho}{2}\left(G_2 + G_3 u + Dv\right) \tag{7b}$$

$$\frac{\partial p}{\partial z} = -\rho\left(g + \frac{\dot{D}}{\varepsilon} - 2\Omega_y u\right) \tag{7c}$$

where

$$G_1 \equiv \dot{D}X - \dot{\zeta}\, Y - D\dot{x}_c + \zeta\, \dot{y}_c + 2\dot{\eta} Z + 2\frac{D}{\varepsilon}\left(\eta + 2\Omega_y\right) \tag{7d}$$

$$G_2 \equiv \dot{D}Y + \dot{\zeta}\, X - \zeta\, \dot{x}_c - D\, \dot{y}_c - 2\dot{\xi}\, Z - 2\frac{D}{\varepsilon}\xi \tag{7e}$$

$$G_3 \equiv \zeta + 4\Omega_z \tag{7f}$$

3.3. SECOND-ORDER PARTIAL DERIVATIVES AND NONLINEAR HARMONIC EQUATIONS

Pressure jumps are known to occur at gust fronts in the surface layer $(z < b)$, as described by Haltiner and Martin [23, pp.305-307]. However, in the midtropospheric layer, we assume that p and its first- and second-order partial derivatives are continuous functions of $x, y,$ and z

(except at radius a, where p must be continuous but its derivatives can be discontinuous). It follows that for $(r < a, b \le z \le h)$

$$\frac{\partial^2 p}{\partial x \partial y} = \frac{\partial^2 p}{\partial y \partial x}, \qquad \frac{\partial^2 p}{\partial x \partial z} = \frac{\partial^2 p}{\partial z \partial x}, \qquad \frac{\partial^2 p}{\partial y \partial z} = \frac{\partial^2 p}{\partial z \partial y} \tag{8}$$

Substituting the cross derivatives of (7a), (7b), and (7c) in (8), dividing by ρ, and setting the coefficients of $X, Y,$ and Z individually to zero in each equation, we obtain the following set of coupled ODE's:

$$\dot{\xi} = \frac{1}{2}\left[\eta(\zeta + 4\Omega_z) - D\xi\right] \tag{9a}$$

$$\dot{\eta} = -\frac{1}{2}\left[\xi(\zeta + 4\Omega_z) + D\eta\right] \tag{9b}$$

$$\dot{\zeta} = -D(\zeta + 2\Omega_z) \tag{9c}$$

$$\dot{D} = \frac{1}{2}\left[\zeta(\zeta + 4\Omega_z) - D^2\right] \tag{9d}$$

$$-\frac{\zeta}{2}(\dot{y}_c - V_b) + \frac{D}{2}(\dot{x}_c - U_b) - \eta\frac{D}{\varepsilon} - \Omega_y\frac{D}{\varepsilon} + 2\Omega_z V_b = 0 \tag{9e}$$

$$\frac{\zeta}{2}(\dot{x}_c - U_b) + \frac{D}{2}(\dot{y}_c - V_b) + \xi\frac{D}{\varepsilon} - \Omega_y\frac{\zeta}{\varepsilon} - 2\Omega_z U_b = 0 \tag{9f}$$

Equations (9e) and (9f) can be solved for the translational velocity of the centerline (in m s^{-1})

$$\dot{x}_c = U_b + \frac{2}{\varepsilon}\Omega_y + \frac{2}{\zeta^2 + D^2}\left[\zeta(-\xi\, w + 2\Omega_z U_b) + D(\eta\, w - 2\Omega_z V_b)\right] \tag{10a}$$

$$\dot{y}_c = V_b + \frac{2}{\zeta^2 + D^2}\left[\zeta\left(-\eta\, w + 2\Omega_z V_b\right) + D\left(-\xi\, w + 2\Omega_z U_b\right)\right] \tag{10b}$$

At the equator where Ω_y is maximal, the term $2\Omega_y / \varepsilon$ in (10a) contributes about 1 m s^{-1} to the translation.

3.4. PRESSURE FIELD

To obtain the inner pressure field p, we first substitute (9) and (1b) in the pressure gradient (7), which gives

$$\frac{\partial p}{\partial x} = -\rho_b{}^0 e^{-\varepsilon Z}\left(1 - B\right)\Omega_y \frac{D}{\varepsilon} \tag{11a}$$

$$\frac{\partial p}{\partial y} = \rho_b{}^0 e^{-\varepsilon Z}\left(1 - B\right)\Omega_y \frac{\zeta}{\varepsilon} \tag{11b}$$

$$\frac{\partial p}{\partial z} = -\rho_b{}^0 e^{-\varepsilon Z}\left(1 - B\right)\left\{g + \dot{w} - 2\Omega_y\left[U_b + \eta Z + \frac{1}{2}\left(DX - \zeta\, Y\right)\right]\right\} \tag{11c}$$

These partial derivatives can now be integrated to obtain p as

$$p(x, y, z, t) = \rho_b{}^0 e^{-\varepsilon Z}\left(1 - B\right)\frac{g}{\varepsilon}\left\{1 + \frac{\dot{w}}{g} - \frac{2\Omega_y}{g}\left[\frac{\eta}{\varepsilon} + U_b + \eta Z + \frac{1}{2}\left(DX - \zeta\, Y\right)\right]\right\} \tag{12}$$

This result shows that the PIO model has no pressure drop at its center, where $X = Y = 0$. A 2-mb pressure drop was measured in the Montana hailstorm. According to Davies-Jones [6], the pressure deficit in mesocyclones is typically about 5 mb. Such a pressure deficit indicates a deviation from the PIO model. Reasons for such deviations are discussed in Section 5.4.

3.5. BALANCE OF FORCES

Equations (9e) and (9f) can be multiplied by ρA, where $A = \pi a^2$, and written in vector form to give a balance of forces per unit length (in N m^{-1})

$$\frac{\rho}{2} A\zeta\, \hat{z} \times (\dot{\mathbf{r}}_c - \mathbf{V}_b) + \frac{\rho}{2} AD(\dot{\mathbf{r}}_c - \mathbf{V}_b) - \rho A\omega \times \hat{z}\, w - A\nabla_H p - 2\rho A\Omega \times \hat{z}\, w - 2\rho A\Omega_z \hat{z} \times \mathbf{V_b} = 0 \tag{13a}$$

where carats denote unit vectors, $\dot{\mathbf{r}}_c \equiv \hat{x}\, \dot{x}_c + \hat{y}\, \dot{y}_c$, $\mathbf{V}_b \equiv \hat{x} U_b + \hat{y} V_b$, and, by (11a), (11b) and (1b)

$$\nabla_H p = -\hat{x}\, \Omega_y \rho \frac{D}{\varepsilon} + \hat{y}\, \Omega_y \rho \frac{\zeta}{\varepsilon} = \hat{z} \times \Omega \rho \frac{D}{\varepsilon} - \hat{z} \times (\hat{z} \times \Omega) \rho \frac{\zeta}{\varepsilon} \tag{13b}$$

The first term is analogous to the Magnus force or Kutta-Joukowski force on a cylinder with a bound vortex of circulation $A\zeta$; differences are a factor of 1/2 and the definition of $\mathbf{V}_b$ as the stationary part of the fluid velocity *inside* the core. The second term is analogous to the force on a source tube of strength AD. The third term is the force exerted by the inner horizontal vorticity on the vertical draft. The fourth term is the force exerted on the core by the horizontal pressure gradient. The fifth term is the Coriolis force on the vertical draft. The last term is the Coriolis force on the stationary part of the flow inside the core.

Thus far, we have reduced the inner solution to a time-dependent set of ODE's, except that we have no equation for $B(t)$ or $a(t)$. These quantities are determined by the jump conditions at the cylindrical interface between the inner and outer solutions, as shown in Figure 1. The cross section is circular only if the model does not translate. For simplicity, we will determine $B(t)$ and $a(t)$ for a nontranslating model and assume that these results apply approximately to the translating model. This assumption will fail if the inner flow does not block the relative environmental wind (Brandes [28]), which will then erode the core.

4. Nontranslating PIO model

4.1. INNER SOLUTION

For the PIO model to remain centered on the origin (*i.e.*, for $\dot{x}_c = \dot{y}_c = 0$), we must take $U_b = V_b = \xi = \eta = \Omega_y = 0$. The velocity (4) and pressure (12) then become in cylindrical coordinates

$$v_r(r,t) = \frac{D(t)}{2} r \tag{14a}$$

$$v_\theta(r,t) = \frac{\zeta(t)}{2} r \tag{14b}$$

$$v_z(t) = w(t) = \frac{D(t)}{\varepsilon} \tag{14c}$$

$$p(z,t) = \rho_b{}^0 e^{-\varepsilon Z} \frac{g}{\varepsilon}[1 - B(t)]\left[1 + \frac{\dot{w}(t)}{g}\right] \tag{14d}$$

4.2. OUTER SOLUTION

With the Rankine vortex as a model, we take the external vorticity ω^0 and divergence D^0 to be zero. Hence, the outer velocity field is given by $(\text{for } r \geq a)$

$$v_r{}^0(r,t) = \frac{D(t)a^2(t)}{2r} \tag{15a}$$

$$v_\theta{}^0(r,t) = \frac{\zeta(t)a^2(t)}{2r} \tag{15b}$$

$$v_z{}^0 = w^0 = 0 \tag{15c}$$

The field v_r is continuous at the interface $r = a(t)$, as required by the jump conditions for the continuity and momentum equations. The field v_θ is also continuous, but $w, \rho, D,$ and ζ all have finite discontinuities. The requirement that the interface move with the fluid gives

$$\dot{a} = \frac{Da}{2} \tag{16}$$

The core buoyancy $B(t)$ can be determined from the jump condition that the pressure be continuous at $r = a$. To determine the outer pressure field, we first solve the momentum equation (6) for the pressure gradient in cylindrical coordinates and then substitute the outer velocity field from (15) and the tendencies from (9c), (9d), and (16) to obtain

$$\frac{\partial p^0}{\partial r} = -\frac{gF\rho^0}{\varepsilon\, r}\left(1 - \frac{a^2}{r^2}\right) \tag{17a}$$

$$\frac{\partial p^0}{\partial \theta} = 0 \tag{17b}$$

$$\frac{\partial p^0}{\partial z} = -g\rho^0 \tag{17c}$$

where F, the Froude number, is given by

$$F = \frac{\varepsilon\, a^2}{4g}\left(\zeta^2 + D^2\right) \tag{17d}$$

As with the inner solution, we require

$$\frac{\partial^2 p^0}{\partial r \partial z} = \frac{\partial^2 p^0}{\partial z \partial r} \qquad (r > a, b \le z \le h) \tag{18}$$

Consequently, the outer density ρ^0 must satisfy

$$\frac{\partial \rho^0}{\partial r} = \frac{F}{\varepsilon\, r}\left(1 - \frac{a^2}{r^2}\right)\frac{\partial \rho^0}{\partial z} \tag{19}$$

The solution of this equation that remains bounded at infinity and satisfies the boundary condition (1a) at $r = a$ is given by

$$\rho^0(r,z,t) = \rho_b{}^0\left(\frac{a}{r}\right)^F \exp\left[-\varepsilon\, Z + \frac{F}{2}\left(1 - \frac{a^2}{r^2}\right)\right] \tag{20}$$

Substituting this result in (17) and integrating for the outer pressure we have the hydrostatic result

$$p^0(r,z,t) = \frac{g}{\varepsilon}\rho^0(r,z,t) = \rho_b{}^0\,\frac{g}{\varepsilon}\left(\frac{a}{r}\right)^F \exp\left[-\varepsilon\, Z + \frac{F}{2}\left(1 - \frac{a^2}{r^2}\right)\right] \tag{21}$$

Because of the smallness of F (Table 1), p^0 and ρ^0 are essentially independent of r within the 60 km radius of validity. As $r \to \infty$, p^0 and ρ^0 slowly approach zero.

4.3. Buoyancy and inner pressure

Equating the outer pressure (21) and the inner pressure (14d) at $r = a$ we obtain

$$B(t) = \frac{\dot{w}(t)}{g} \tag{22}$$

This expression is similar to that given by Darkow [29] for the vertical acceleration of a nonentraining buoyant parcel. The inner pressure is now independent of t and given by

$$p(z) = \rho_b{}^0\,\frac{g}{\varepsilon}e^{-\varepsilon Z} \tag{23}$$

By (9d), the buoyancy (22) can also be written

$$B = \frac{1}{2\varepsilon g}\left[\zeta\left(\zeta + 4\Omega_z\right) - D^2\right] \tag{24}$$

4.4. SUPPLEMENTARY FORMULAS

Although the model is now complete, formulas for certain additional quantities will be useful for comparison with meteorological data. The mesocyclonic circulation Γ is given by (in $m^2\ s^{-1}$)

$$\Gamma = \pi\, a^2 \zeta \tag{25}$$

The net mass influx M at cloud base b is given by (in kg s^{-1})

$$M = \pi\, a^2 w \rho_b{}^0 (1 - B) \tag{26}$$

As mentioned earlier, the outer temperature T^0 in the model is a constant; its value is given by

$$T^0 = \frac{g}{\varepsilon\, R} \tag{27}$$

where R, the gas constant, equals 287 J kg^{-1} K^{-1}. The inner temperature T is given by

$$T(t) = T^0\left[1 + B(t)\right] \tag{28}$$

Thus, the model core is also isothermal, but its temperature varies with the buoyancy.

The energy equation, as given by Holton [5, p. 51], can be written

$$q = \rho\, c_p \left(\frac{\partial}{\partial t} + \mathbf{v}\cdot\nabla\right) T - \left(\frac{\partial}{\partial t} + \mathbf{v}\cdot\nabla\right) p \tag{29}$$

where q (in W m^{-3}) is the diabatic heating rate, which in the PIO model is due only to latent energy release, and c_p equals 1004 J kg^{-1} K^{-1}. Substituting the inner pressure (23) and temperature (28) and integrating over the core, we obtain the total heating rate Q (in W) required to support the PIO

$$Q = \rho_b{}^0 \frac{\pi a^2}{\varepsilon}\left[c_p T^0 \dot{B} + w\left(c_p \frac{\partial T}{\partial z} + g\right)\right]\left[1 - e^{-\varepsilon(h-b)}\right] \tag{30a}$$

Although the model troposphere is isothermal between b and h, we have retained $\partial T / \partial z$ to be more accurate when applying this formula to an actual supercell. The corresponding net water vapor influx M_v (in g s^{-1}) is given by

$$M_v = \frac{Q}{L_c} \tag{30b}$$

where L_c, the latent heat of condensation, equals 2.5×10^3 J g^{-1}.

5. Nondimensionalization and analytic solution

5.1. NONDIMENSIONALIZATION

We define dimensionless (primed) variables by

$$t' = 2\Omega_z t \tag{31a}$$

$$(\xi', \eta', \zeta', D') = \frac{1}{2\Omega_z}(\xi, \eta, \zeta, D) \tag{31b}$$

(where we will use ζ' interchangeably with the Rossby number Ro)

$$B' = \frac{\varepsilon g B}{2\Omega_z{}^2} = \frac{\varepsilon g\left(T - T^0\right)}{2\Omega_z{}^2 T^0} \tag{31c}$$

$$a' = \frac{a}{a_0} \tag{31d}$$

where subscript 0 denotes an initial value at $t' = 0$.

The model Equations (9a)-(9d), (24), (16), and (5) can then be written in dimensionless form, as follows

$$2\frac{d\xi'}{dt'} = \eta'(\zeta'+2) - D'\xi' \tag{32a}$$

$$2\frac{d\eta'}{dt'} = -\xi'(\zeta'+2) - D'\eta' \tag{32b}$$

$$\frac{d\zeta'}{dt'} = -D'(\zeta'+1) \tag{32c}$$

$$2\frac{dD'}{dt'} = \zeta'(\zeta'+2) - D'^2 \tag{32d}$$

$$B' = \zeta'(\zeta'+2) - D'^2 \tag{32e}$$

$$\frac{da'}{dt'} = \frac{D'a'}{2} \tag{32f}$$

$$\frac{d\theta}{dt'} = \frac{\zeta'}{2} \tag{32g}$$

5.2. Analytic solution

Equations (32c) and (32d) uncouple from the other equations. Although this pair is nonlinear, the equation for $dD'/d\zeta'$ is linear in D'^2 and leads to an analytic solution. Subject to the initial conditions $D'(0) = 0$ and $\zeta'(0) = \zeta_0'$, the analytic solution is given by

$$\zeta'(t') = \frac{\cos t' - \dfrac{\zeta_0'}{\zeta_0'+2}}{1 + \dfrac{2}{\zeta_0'(\zeta_0'+2)} - \cos t'} \tag{33a}$$

$$D'(t') = \frac{\zeta_0'(\zeta_0'+2)\sin t'}{|\zeta_0'(\zeta_0'+2)\sin t'|}\sqrt{(\zeta_0' - \zeta')\left(\zeta' + \frac{\zeta_0'}{\zeta_0'+1}\right)} \tag{33b}$$

Equations (32c), (32d), and (32f) yield, with $a'(0) = 1$

$$a'(t') = \frac{|\zeta_0'|}{\sqrt{\zeta'^2 + D'^2}} \tag{33c}$$

from which it follows that the Froude Number F, as given by (17d), is a constant of the motion. By (32a), (32b), and (32f), we have $\sqrt{\xi'^2 + \eta'^2} = \frac{1}{a'}\sqrt{\xi_0'^2 + \eta_0'^2}$, which shows that the magnitude of the inner horizontal vorticity vector is inversely proportional to the core radius. Integration of (32g) gives, with $\theta(0) = 0$

$$\theta(t') = \frac{\zeta_0' + 1}{|\zeta_0' + 1|} \arctan\left[|\zeta_0' + 1| \tan\left(\frac{t'}{2}\right)\right] - \frac{t'}{2} \tag{33d}$$

Plots of D' versus ζ' and ζ', D', B', a', and θ versus t' are shown in Figure 2 for $\zeta_{10}' = -0.814$ (Montana hailstorm simulation) and $\zeta_{20}' = -1.186$. In the (ζ', D') phase plane, there are equilibrium points at $(0,0)$ and $(-2,0)$. The point (0,0) is the center for an oscillation that gives cyclonic pulses and (-2,0) is the center for anticyclonic pulses. The line $\zeta' = -1$ separates these two oscillations and represents infinite contraction and spin-up for both. Since initial values ζ_0' are chosen along the line $D' = 0$, two values of ζ_0' give the same solution, except that the pulses are displaced by π. (Had we chosen $\zeta_{10}' = 4.39$ and $\zeta_{20}' = -6.39$, the same pulses in Figure 2 would have occurred at $t' = 0, \pm 2\pi, \ldots$) Cyclonic and anticyclonic spin-up both occur in a contracting downdraft. The downdraft reverses in the middle of a pulse and spin-down occurs in an expanding updraft. This draft reversal results from a pulse of positive buoyancy.

5.3. EXTREMA FORMULAS, ETC.

Values of the fields at $t' = 0$ and $t' = \pi$ are related as follows:

$$\zeta'(\pi) = \frac{-\zeta_0'}{\zeta_0'+1} \tag{34a}$$

$$\zeta_0' = \frac{-\zeta'(\pi)}{\zeta'(\pi)+1} \tag{34b}$$

$$D_0' = D'(\pi) = 0 \tag{34c}$$

$$B_0' = \zeta_0'(\zeta_0'+2) \tag{34d}$$

$$B'(\pi) = \frac{-\zeta_0'(\zeta_0'+2)}{(\zeta_0'+1)^2} \tag{34e}$$

$$a'(\pi) = |\zeta_0'+1| \tag{34f}$$

The fields $D', B',$ and $\theta_{cyclonic}$ have extrema that occur at intermediate times:

$$D'_{\max} = \left|\frac{\zeta_0'(\zeta_0'+2)}{2(\zeta_0'+1)}\right| \tag{34g}$$

$$D'_{\min} = -D'_{\max} \tag{34h}$$

$$B'_{\min} = \frac{-(\zeta_0'^2+2\zeta_0'+2)^2}{8(\zeta_0'+1)^2} \tag{34i}$$

$$\theta_{\max} = \left|\arctan\sqrt{\zeta_0'+1} - \arctan\frac{1}{\sqrt{\zeta_0'+1}}\right| \quad (\zeta_0' > -1) \quad \text{cyclonic pulse} \tag{34j}$$

$$\theta_{\min} = -\theta_{\max} \quad (\zeta_0' > -1) \quad \text{cyclonic pulse} \tag{34k}$$

As the intensity of a cyclonic pulse increases, $\theta_{\max} \to \pi/2$; hence the total angular excursion of the core fluid $(\theta_{\max} - \theta_{\min}) \to \pi$.

The dimensionless time interval to spin up a cyclonic peak from $\zeta' = 0$ is given by

$$\Delta t'_{spin-up} = \arccos\left(\frac{\zeta_0'}{\zeta_0'+2}\right) \quad (0 \le \zeta_0') \tag{34l}$$

As the pulse amplitude increases, the spin-up time *decreases*. This feature is typical of nonlinear oscillations [30].

Since the limiting factor on the amplitude of a pulse is the core buoyancy, it is useful to rewrite some of the preceding relations in terms of the initial buoyancy B_0', where $B_0' > -1$, as follows:

$$\zeta_0' = -1 + \sqrt{1 + B_0'} \quad \text{(cyclonic pulse)} \tag{35a}$$

$$\zeta_0' = -1 - \sqrt{1 + B_0'} \quad \text{(anticyclonic pulse)} \tag{35b}$$

$$B'(\pi) = \frac{-B_0'}{1 + B_0'} \tag{35c}$$

$$D'_{\max} = \frac{|B_0'|}{2\sqrt{1 + B_0'}} \tag{35d}$$

$$B'_{\min} = \frac{-(2 + B_0')^2}{8(1 + B_0')} \tag{35e}$$

Equation (35e) shows that as the pulse amplitude gets large, the positive peaks of $B'(t')$ become 8-times greater than its negative peaks.

5.4. MAXIMUM VORTICITY AND UPDRAFT SPEED

In this section, we apply the PIO model to an intense vertical draft in the interior of a supercell storm. The objective is to see if the PIO can reproduce a hail-producing updraft of $w \approx 50\ \mathrm{m\ s^{-1}}$ or a tornadic vortex of Rossby number $\mathrm{Ro} \approx 1000$. As mentioned, we limit the temperature excess in the core $(T - T^0)$ to the range $(-12\ \mathrm{K} \le T - T^0 \le 12\ \mathrm{K})$. The parameters for the Montana hailstorm are listed in Table 1: $\Omega_z = 5.2623 \times 10^{-5}\ \mathrm{s^{-1}}$, $\varepsilon = 1.19 \times 10^{-4}\ \mathrm{m^{-1}}$, and $T^0 = 287$ K. Taking $T - T^0 = 12$ K in (31c), we obtain $B'_{\max} = B_0' = 8.81 \times 10^3$. Equations (35a) and (35d) then give $\zeta_0' = \zeta'_{\max} = \mathrm{Ro}_{\max} = 92.9$ and $D'_{\max} = 46.9$, from which we obtain $\zeta_{\max} = 9.78 \times 10^{-3}\ \mathrm{s^{-1}}$ and $w_{\max} = 41.5\ \mathrm{m\ s^{-1}}$.

This value for w_{max} is 17 percent short of the goal. The value for ζ_{max}, although triple the maximum vorticity of 3×10^{-3} s^{-1} measured in the interior of the Montana hailstorm (Section 7.1), is an order of magnitude less than the goal of a tornadic vortex. However, the 8 to 1 asymmetry between positive and negative peaks of buoyancy in result (35e) has indicated something new to try: In the preceding calculation, we took the minimum dimensionless buoyancy $B'_{min} = -1.1\times10^{3}$, for which $T - T^0 = -1.5$ K. If, instead, we take $B'_{min} = -8.81\times10^{3}$, which corresponds to the negative limit $T - T^0 = -12$ K, then the positive extremum B'_{max} will be far off the allowable scale. Since the PIO goes through negative values of buoyancy first, it could proceed until it encounters the positive limit $(T - T^0 = 12\,\mathrm{K})$. Then the PIO would stall, leaving the internal draft in a state of prolonged downflow, contraction and spin-up – a scenario that should produce a higher Rossby number. A different stall scenario could increase the updraft speed and also explain the 5 mb central pressure deficit typically observed for mesocyclones. After any stall, however, the problem requires a different formulation that is beyond the present scope.

6. Physical nature of PIO

6.1. INERTIAL FLOW

We present a simple physical picture for the two oscillations shown in Figure 2. The model is nontranslating. The period π / Ω_z (in s), which is half the period of a Foucault pendulum, suggests that the oscillations are inertial. As described by Holton [5, pp. 64-65] and Haltiner and Martin [23, pp. 178-181], inertial flow is frictionless horizontal flow in which a fluid parcel moves with constant speed v_i along an arc such that the centrifugal force balances the Coriolis force. The horizontal pressure gradient $\nabla_H p$ is zero – which agrees with the absence of a central pressure deficit in the PIO model. The radius r_i of the arc is given by (in m) $r_i = v_i / 2\Omega_z$ and the motion is anticyclonic. Since we take Ω_z constant, the parcel traverses a circle, as shown in Figure 3(a). Introducing the dimensionless coordinates $r_i' = r_i / a_0$ and $v_i' = v_i / 2\Omega_z a_0$ we have $r_i' = v_i'$.

6.2. CORE CONTRACTION AND SPIN-UP

We now consider the fields in Figure 2 at $t'=0$. Figure (3b) is an aerial view of the dimensionless core at this time. The velocity of parcels on the periphery is given by $v_i'=-\zeta_0'/2$. The inertial radius of these parcels, $r_i'=-\zeta_0'/2$, is also shown. The physical explanation for the cyclonic pulses in Figure 2 is as follows: Figure 3(c) shows the inertial arcs for $\zeta_0'=-0.8\,14$ during the first half period $(0\le t'\le\pi)$ when the core contracts and spins up cyclonically. As the core contracts, the parcels are compressed by descending in a negatively buoyant downdraft. The negative buoyancy results from evaporative cooling of moisture deposited in the middle troposphere by a previous updraft. This downdraft reverses at $t'=\pi$ because of a pulse of positive buoyancy from condensational heating of moist low level air that is lifted by the gust front of the downdraft. Figure 3(d) shows the complete cycle including spin-down in an expanding updraft. Although we have only followed parcels on the periphery, every parcel in the core simultaneously traverses a similar inertial circle.

The anticyclonic pulses in Figure 2 have a similar explanation. Figure 3(e) shows the inertial arcs for $\zeta_0'=-1.186$, where the core contracts and spins up anticyclonically. The vertical speed and buoyancy are the same as for cyclonic spin-up. A singularity occurs as $r_i'\to 0.5$ $(\text{or } \zeta_0'\to -1)$ that corresponds to infinite contraction and spin-up. In the troposphere, this mathematical singularity is avoided because of physical limitations on the buoyancy.

6.3. BLOCKING MESO-ANTICYCLONE

Finally, if $r_i'=1$ $(\text{or } \zeta_0'=-2)$, we obtain a steady meso-anticyclone. (The full set of model equations shows that $\dot{x}_c=2\Omega_y/\varepsilon$, $\dot{y}_c=D=w=B=Q=0$, and that a,ξ,η,U_b, and V_b are arbitrary constants, subject to the constraint that the core not be eroded. The meso-anticyclone translates eastward at about one-tenth the speed of weather patterns and, therefore, would have a blocking effect.)

7. Application to Montana hailstorm

7.1. STORM DESCRIPTION

Our second study compares the PIO model with data from the Montana hailstorm. This storm initially appeared on radar inside the CCOPE mesonetwork at about 0030 UTC on 12 July 1981. The midpoint of the right turn in its track occurred at 0200 UTC. Between 0206 and 0209 UTC, three Doppler radars measured an interior vorticity maximum of 3×10^{-3} s^{-1}. At 0211 UTC, the supercell was producing baseball- to grapefruit-size hail. At about 0250 UTC, it moved off the mesonetwork and evolved into a mesoscale convective complex. We hypothesize that the PIO started sometime between 0030 and 0100 UTC, proceeded through one pulse, and stopped shortly after 0250 UTC.

7.2. INITIAL VALUES AND PARAMETERS

The initial values and other parameters used in the PIO model to simulate this hailstorm are listed in Table 1, where $t = 0$ coincides with the midpoint of a pulse. Dimensionless plots for $\zeta', D', B', a',$ and θ are already given by the cyclonic pulses in Figure 2 with a trivial shift of the t'-origin. Besides these plots from the analytic solution, we numerically integrate (9a), (9b), and (10) to obtain $\xi(t), \eta(t)$ and $x_c(t), y_c(t)$, which are plotted in Figure 4. (The numerical procedure is a fourth order Runge-Kutta-Fehlberg code. The time step is automatically adjusted within the range 10^{-11} to 1, subject to an error tolerance of 10^{-6} per step.) The five solid triangles in Figures 2, 3(d), and 4 relate the simulation to universal time during the hailstorm. The average vertical draft in the model is also tested qualitatively against surface mesonetwork data at these five times.

The initial values in Table 1 were chosen as follows: As shown in Figures 2(b) and 4(b), the midpulse is coincident with the center of the turn and, therefore, occurs at 0200 UTC. The minimum core radius a_0 was chosen to include the 40 dBZ low level radar echo at 0200 UTC so that the core would capture the major convection as well as the mesocyclonic vorticity. The initial value ζ_0, which determines the degree of nonlinearity, was chosen so that $a(t)$ replicates the growth rate of the radar echoes after 0200 UTC, as given by [20]. The initial

values ζ_0, η_0 and the constants U_b, V_b were chosen to simulate the time track of the mesocyclone. The PIO time track from Figure 4(b) is shown superimposed on the observed time track in Figure 5, where fairly good agreement is evident.

With these initial values, the model computes the peak mesocyclonic circulation Γ as 2.8×10^5 m^2 s^{-1} at 0200 UTC. Although Γ was not reported for the Montana storm, the computed value compares with a typical value of 5×10^5 m^2 s^{-1}, as given by Davies-Jones [6]. The net mass influx M at cloud base is computed as 1.32×10^9 kg s^{-1} at 0230. This quantity was not reported either; however, the computed value compares well with a measured value of 1.3×10^9 kg s^{-1} for M during a similar time in the Colorado hailstorm. The model computes the net water vapor influx M_v at 0230 as 4.2×10^9 g s^{-1}. This value compares with a measured value of 8.5×10^9 g s^{-1} -- again from the Colorado hailstorm. According to our simulation, M_v continues to rise after 0230. We speculate that the PIO stops shortly after 0250 UTC partly because the net water vapor influx required to maintain it becomes too large.

7.3. Comments on time track, etc.

The eastward drift of the kidney-shaped track shown in Figure 4(b) results from the term $2\Omega_y / \varepsilon$ in (10a). The upper (westward) track segments that occur between the pulses are not observed for supercells and are included only to show the complete oscillation. These upper segments suggest a second reason for the PIO to stop shortly after a pulse. As the track turns toward the north and eventually toward the west, the relative environmental wind increases. The inner flow can no longer block the relative environmental wind, which then erodes the core. Incidentally, we take h = 6.3 km in Table 1 because a vertical radar section appears to show substantial core erosion above this height [20].

We seek an explanation for the right turn in the track at 0200 UTC. Figure 4(a) shows that the average horizontal vorticity vector rotates clockwise about ¼ turn from 0130 to 0230 UTC with ξ changing from negative to positive at about 0200 UTC. The average vertical draft w also changes from negative to positive at 0200, as shown in Figure 2(c). Equation (10b) for $\dot{y}_c$ confirms that these sign reversals in w and ξ cause the right turn in the track. (If the

model is run with $\xi_0 = \eta_0 = 0$, no turn at all occurs at 0200 UTC.) Newton and Newton [31], Rotunno and Klemp [25], and others have also linked the right turn in the track to horizontal vorticity but not to a reversal of the average vertical draft.

Besides the time track, Figure 5 shows the model core at the five times. Figure 6 shows the corresponding low level radar echoes. The core approximately matches the 40 dBZ radar echo at 0200 UTC. However, at earlier times, 0130, 0100, and 0030 UTC, the model core is substantially larger than the corresponding radar echo. We conclude that much of the average downdraft predicted by the PIO model during this earlier period would have been invisible to radar.

(The individual radar scans shown in Figure 6 were begun at 0030:36, 0102:05, 0132:05, 0202:19, and 0232:14 UTC on 12 July 1981. The scan at about 0030 UTC was taken at 0.5^{o} elevation by the NCAR CP-2 radar (10-cm wavelength) located at (0,0) km on the x,y coordinate frame shown. (The origin of the coordinate frame is located at 46^{o} 25' 56" N lat and 105^{o} 56' 10" W long.) The remaining scans were taken at 1^{o} elevation by the Bureau of Reclamation Skywater radar (5-cm wavelength) located at (2.5,-2.2) km. The reflectivity grayscale shown to the right of each figure goes from 10 to 60 dBZ.)

8. Comparison of the PIO and conventional models with surface mesonetwork data

8.1. CRITICAL DATA

The salient feature of the PIO model is the contracting average downdraft that spins up the mesocyclone with help from the Coriolis force. This downdraft occurs before the track turns to the right -- before 0200 UTC for the Montana hailstorm. After 0200, the average draft becomes upward. In the conventional model, the average vertical draft is upward from storm inception until dissipation.

Relevant data before the right turn are not easy to find. If the downdraft should contain little condensed water, it would be invisible to the eye and camera as well as to radar. This downdraft could be detected by aircraft wind measurements; but, as shown by Foote and Fankhauser [19], it takes aircraft about 45 min to circumnavigate a storm. Once a probable

supercell is identified, little time is left for aircraft to reach it and make measurements before the right turn. At present, the only way of detecting this downdraft appears to be with a surface mesonetwork. The average downdraft would cause an average divergent flow near the surface that could be detected by the wind sensors. Conversely, an average updraft would cause an average convergent flow.

Surface data alone are not conclusive. Multilevel wind data between the surface and cloud base (1.5 km above the surface for the Montana storm) are needed to measure the net mass influx at cloudbase. Such multilevel wind data could be obtained by a mesonetwork composed of wind profilers operating in conjunction with Doppler radars. The wind profilers would function in the clear air and the Doppler radars in the precipitation regions. Until such data become available, however, surface data appear to be the only means for testing the average vertical draft sequences in the PIO and conventional models.

8.2. UNIQUE DATA SET

After forming inside the CCOPE mesonetwork, the Montana hailstorm traversed the southern part of the network where the mesh size was about 20 km and the wind sensors were mounted 6 m above ground level (AGL). Hence, the term "surface" as we will use it actually denotes 6 m AGL. Surface winds were recorded every 5 min at each operating station. The recorded values were time averages of data taken during the previous 5 min. Sample vector plots of these recorded surface winds were made every half hour. These plots were obtained on 35-mm microfilm, entitled "CCOPE PROBE Data -- A First Look," from the National Center for Atmospheric Research in Boulder, Colorado, USA.

8.3. SURFACE DATA ANALYSIS METHOD

We analyzed these plotted surface wind data at 0030, 0100, 0130, 0200, and 0230 UTC on 12 July 1981. The analysis was done graphically on 25 by 25-cm prints. A polygon was drawn on network points that surround the center of the mesocyclone at each of these five times, as shown in Figure 6. The vertices were taken 20 to 40 km from the mesocyclone center. This size was needed to accommodate the 20-km mesh size and to capture the model core shown in Figure 5.

Some network stations were inoperative or only partially operative when this storm passed through; the resulting absence of data caused irregularities in some of the polygons.

8.4. AVERAGE HORIZONTAL DIVERGENCE VERSUS t

The average horizontal divergence $\langle D \rangle_{sfc}$ on the surface polygons is plotted versus t in Figure 7. Positive $\langle D \rangle_{sfc}$ indicates an average downdraft just above the surface. Similarly, negative $\langle D \rangle_{sfc}$ indicates an average updraft just above the surface. According to Wade [22], the error in the surface wind measurements was 0.5 m s^{-1}. The error bars in Figure 7 were determined by using this value in an error formula given by Davies-Jones [32].

Figure 7 supports the PIO hypothesis. The transition from average updraft at 0030 UTC to average downdraft at 0100 UTC suggests that the PIO started during this interval. The average downdraft continued until about 0200 UTC, when it changed to an average updraft, in qualitative agreement with the PIO model

8.5. DRAFT STRUCTURE AND TIME DEPENDENCE

Further details of the measured vertical draft were obtained by using interior grid points to divide each polygon into triangles. When the horizontal divergence was computed on each triangle, coexistent updrafts and downdrafts were resolved. In particular, at 0200 UTC, we found a forward- and a rear-flank downdraft. These dual downdrafts are typical of well-developed supercell storms, as shown by Miller et al. [24] and Davies-Jones [6].

If the measured horizontal divergence on each triangle is multiplied by its area, we obtain the horizontal efflux E_{sfc} (in m^2 s^{-1}). These effluxes are additive and can be plotted separately for the downdraft, updraft, and net draft as done in Figure 8. This figure highlights the coexistence of updrafts and downdrafts. The updrafts, subjected to vertical windshear, could continuously supply moisture to the middle troposphere for evaporatively cooling the downdrafts. Figure 8 shows that the reversal in net draft at about 0200 UTC was caused by a rapid growth of the updraft.

9. Conclusions

The pulsing inertial oscillation (PIO) model is a nonlinear, time-dependent, translating vortex solution of the inviscid, compressible fluid dynamic equations in the middle troposphere. A property of this model is that vertical windshear causes the track of a cyclonic vortex to turn to the right during a pulse and that of an anticyclonic vortex to turn to the left. Such translation is typical of supercell storms -- rotating thunderstorms that can generate tornadoes and hail.

Two studies were made to test the hypothesis that some supercell storms are manifestations of a PIO pulse. The first study applied the PIO model to an intense internal draft. The objective was to simulate a hail producing updraft ≈ 50 m s^{-1} and a tornadic vortex -- a vortex aloft of Rossby number ≈ 1000 that precedes development of a tornado at the surface. The draft buoyancy was limited by practical considerations to a temperature excess of ± 12 K. Subject to this limitation, the PIO produced a maximum updraft speed of 41.5 m s^{-1} and a Rossby number of 92.9. However, the high degree of asymmetry between the positive and negative values of buoyancy required to support the PIO suggest that the PIO could easily get stalled in a state of prolonged downdraft, contraction, and spin-up. Such a stall could increase the Rossby number. A different stall scenario could increase the updraft speed and also explain the 5 mb central pressure deficit typically observed for mesocyclones. To explore these promising options, however, requires an advanced model that would apply after a stall has occurred.

The second study applied the PIO model to a supercell storm as a whole. The model successfully simulated bulk properties such as the mesocyclonic circulation, the net mass and moisture influxes, and the time track. Moreover, we found a critical feature of the PIO model to test against storm data. The average vertical draft is downward before the turn in the track and upward afterwards. This feature of the PIO model contrasts with the conventional model, in which the average vertical draft is upward from storm inception until dissipation.

Surface mesonetwork data were found to be the best data available for testing the vertical draft sequences in the PIO and conventional models. Data from a hailstorm that occurred during

the 1981 Cooperative Convective Precipitation Experiment (CCOPE) in southeastern Montana, USA, support the PIO model. However, surface data alone are not conclusive, and further measurements are needed. A mesonetwork consisting of wind profilers operating in conjunction with Doppler radars would yield multilevel data that are conclusive.

Acknowledgements

One of the authors (R.C.C.) thanks Edmund J. Conway, Joel S. Levine, and Dennis M. Bushnell for their support. He thanks one of the referees, L. K. Forbes of the University of Queensland, Australia, for helping obtain an analytic solution of the reduced equations. He thanks Larry V. Stock for writing the computer code and Lona M. Howser, John T. Bowen, and Mary M. Johnson for updating it. He thanks Fred H. Proctor for identifying the oscillation as inertial, his wife, Barbara, for naming the oscillation, and many colleagues for helpful discussions. He thanks T. Theodore Fujita of The University of Chicago and Charles G. Wade, William D. Anderson, and Toni A. Biter of the National Center for Atmospheric Research for help in obtaining a suitable surface mesonetwork data set. We thank Eloise L. Johnson for editing the manuscript and Anne C. Costa and Leanna D. Bullock for preparing the figures.

References

1. T. Fujita and H. Grandoso, Split of a thunderstorm into anticyclonic and cyclonic storms and their motion as determined from numerical model experiments. *J. Atmos. Sci.*, 25 (1968) 416-439.
2. W. Ferrel, *A Popular Treatis on the Winds*. John Wiley. New York (1889) 505 pp.
3. J. M. Wallace and P. V. Hobbs, *Atmospheric Science, An Introductory Survey.* Academic Press. New York (1977) 467 pp.
4. B. R. Morton, Geophysical vortices. *Progress in Aeronautical Sciences*, Vol. 7, D. Kuchemann, Ed. Pergamon Press (1966) 145-194.
5. J. R. Holton, *An Introduction to Dynamic Meteorology*. Third edition. Academic Press (1992) 511 pp.

6. R. P. Davies-Jones, Tornado dynamics. *Thunderstorm Morphology and Dynamics*, Second Edition. E. Kessler, Ed. Vol. 2. *Thunderstorms: A Social, Scientific, and Technological Documentary*, Univ. of Oklahoma Press. London (1986) 197-236.
7. L. Bengtsson and J. Lighthill (Eds.), *Intense Atmospheric Vortices.* Springer-Verlag. Heidelberg (1982) 326 pp.
8. E. Kessler (Ed.), *Thunderstorm Morphology and Dynamics.* Second edition. Vol. 2. *Thunderstorms: A Social, Scientific, and Technological Documentary.* Univ. of Oklahoma Press. London (1986).
9. P. S. Ray (Ed.), *Mesoscale Meteorology and Forecasting.* Amer. Meteor. Soc. (1986) 793 pp.
10. J. B. Klemp, Dynamics of tornadic thunderstorms. *Ann. Rev. Fluid Mech., 19* (1987) 369-402.
11. C. Church, D. Burgess, C. Doswell, and R. Davies-Jones (Eds.), *The Tornado: Its Structure, Dynamics, Prediction, and Hazards.* Geophysical Monograph 79. American Geophysical Union (1993) 637 pp.
12. R. E. Schlesinger, A three-dimensional numerical model of an isolated deep thunderstorm. Part II: Dynamics of updraft splitting and mesovortex couplet evolution. *J. Atmos. Sci.,* 37 (1980) 395-420.
13. R. A. Brown, Initiation and evolution of updraft rotation within an incipient supercell thunderstorm. *J. Atmos. Sci.*, 49 (1992) 1997-2014.
14. R. A. Maddox, An evaluation of tornado proximity wind and stability data. *Mon. Wea. Rev.*, 104 (1976) 133-142.
15. J. B. Klemp and R. B. Wilhelmson, Simulations of right- and left-moving storms produced through storm splitting. *J. Atmos. Sci., 35* (1978) 1097-1110.
16. D. K. Lilly, The development and maintenance of rotation in convective storms. *Intense Atmospheric Vortices.* L. Bengtsson and J. Lighthill, Eds. Springer-Verlag. Heidelberg (1982) 149-160.

17. L. J. Wicker and R. B. Wilhelmson, Simulation and analysis of tornado development and decay within a three-dimensional supercell thunderstorm. *J. Atmos. Sci.*, 52 (1995) 2675-2703.

18. R. C. Costen and L. V. Stock, Inertial oscillation of a vertical rotating draft with application to a supercell storm. NASA TP-3230 (1992) 47 pp. with 8-minute video supplement available.

19. G. B. Foote and J. C. Fankhauser, Airflow and moisture budget beneath a northeast Colorado hailstorm. *J. Appl. Meteor.*, 12 (1973) 1330-1353.

20. J. C. Fankhauser, G. M. Barnes, L. J. Miller, and P. M. Roskowski, Photographic documentation of some distinctive cloud forms observed beneath a large cumulonimbus. *Bull. Amer. Meteor. Soc.*, 64 (1983) 450-462.

21. C. A. Knight (Ed.), The cooperative convective precipitation experiment (CCOPE), 18 May -7 August 1981. *Bull. Amer. Meteor. Soc.*, 63 (1982) 386-398.

22. C. G. Wade, A quality control program for surface mesometeorological data. *J. Atmos. Ocean. Technol.*, 4 (1987) 435-453.

23. G. J. Haltiner and F. L. Martin, *Dynamical and Physical Meteorology.* McGraw-Hill. New York (1957) 470 pp.

24. L. J. Miller, J. D. Tuttle, and C. A. Knight, Airflow and hail growth in a severe northern high plains supercell. *J. Atmos. Sci.*, 45 (1988) 736-762.

25. R. Rotunno and J. B. Klemp, The influence of the shear-induced pressure gradient on thunderstorm motion. *Mon. Wea. Rev.*, 110 (1982) 136-151.

26. D. K. Lilly, The structure, energetics and propagation of rotating convective storms. Part II: Helicity and storm stabilization. *J. Atmos. Sci.* 43 (1986) 126-140.

27. W. Menke and D. Abbott, *Geophysical Theory*. Columbia Univ. Press New York (1990) 458 pp.

28. E. A. Brandes, Finestructure of the Del City-Edmond tornadic mesocirculation. *Mon. Wea. Rev.*, 109 (1981) 635-647.

29. G. L. Darkow, Basic thunderstorm energetics and thermodynamics. *Thunderstorm Morphology and Dynamics.* Second edition. E. Kessler, Ed. Vol. 2. *Thunderstorms: A Social, Scientific, and Technological Documentary*, Univ. of Oklahoma Press. London (1986) 59-73.

30. M. Urabe, *Nonlinear Autonomous Oscillations*. Academic Press (1967) 330 pp.

31. C. W. Newton and H. R. Newton, Dynamical interactions between large convective clouds and environment with vertical shear. *J. Meteor.*, 16 (1959) 483-496.

32. R. Davies-Jones, Useful formulas for computing divergence, vorticity, and their errors from three or more stations. *Mon. Wea. Rev.*, 121 (1993) 713-725.

Table 1. Initial values and parameters used in PIO model for Montana hailstorm.

$\xi(0)$, s^{-1}	1.05×10^{-4}
$\eta(0)$, s^{-1}	9.95×10^{-4}
$\zeta(0)$, s^{-1}	4.62×10^{-4}
$D(0)$, s^{-1}	0
$w(0)$, m s^{-1}	0
$a(0)$, km	13.9
$\theta(0)$, rad	0
$x_c(0)$, m	0
$y_c(0)$, m	0
U_b, m s^{-1}	10.85
V_b, m s^{-1}	-2.27
[a] Ω_y, rad s^{-1}	5.0479×10^{-5}
[a] Ω_z, rad s^{-1}	5.2623×10^{-5}
[a] b, km MSL[b]	2.5
[a] h, km MSL[b]	6.3
[a] $\rho_b{}^0$, kg m^{-3}	0.92
[a,c] $p(b)$, kPa	75.5
g, m s^{-2}	9.81
[d] ε, m^{-1}	1.19×10^{-4}
F	2.03×10^{-4}
T^0, K	287
[c] $T(b)$, K	287
[c] $T(h)$, K	260
$\partial T/\partial z$, K m^{-1}	-7.2×10^{-3}
R, J kg^{-1} K^{-1}	287
c_p, J kg^{-1} K^{-1}	1004
L_c, J g^{-1}	2.5×10^3

[a]Fankhauser *et al.* [20]. [b]Above mean sea level (MSL). [c]Sounding from Baker, Montana, at 0110 UTC 12 July 1981 (see also Fig. 5). [d]From (23) at height $z = b$

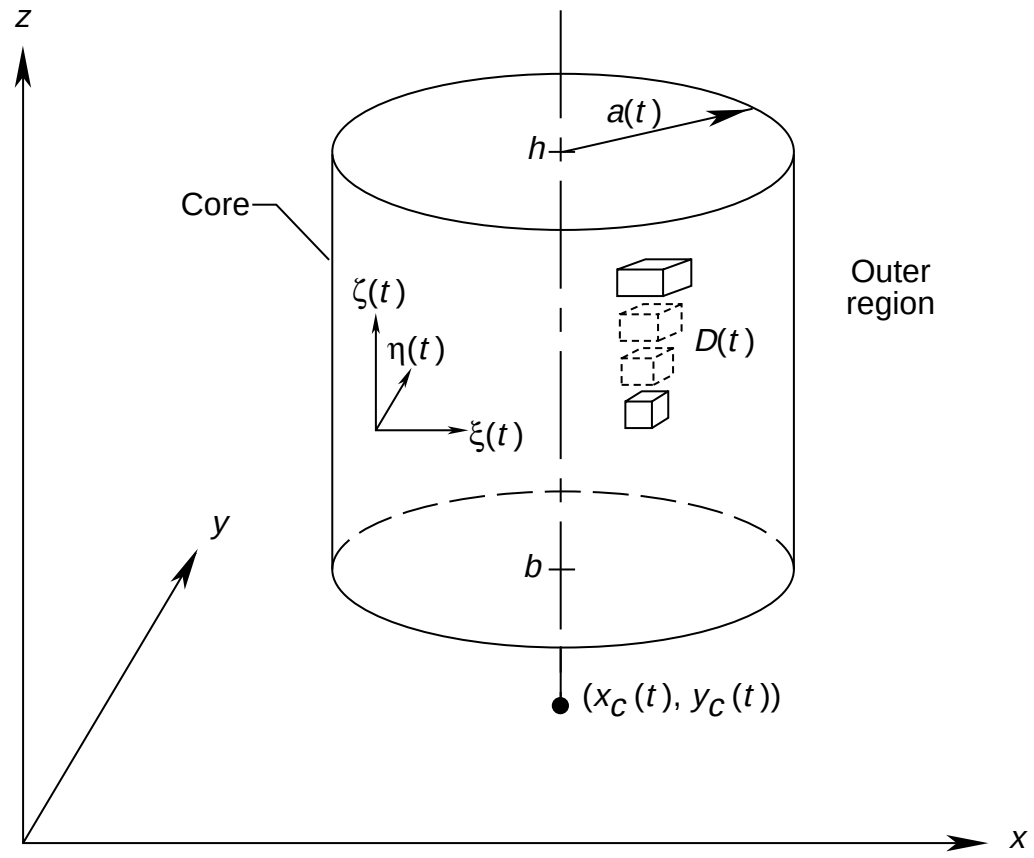

Figure1. Pulsing inertial oscillation (PIO) model for convective core of a supercell storm or an intense internal draft.

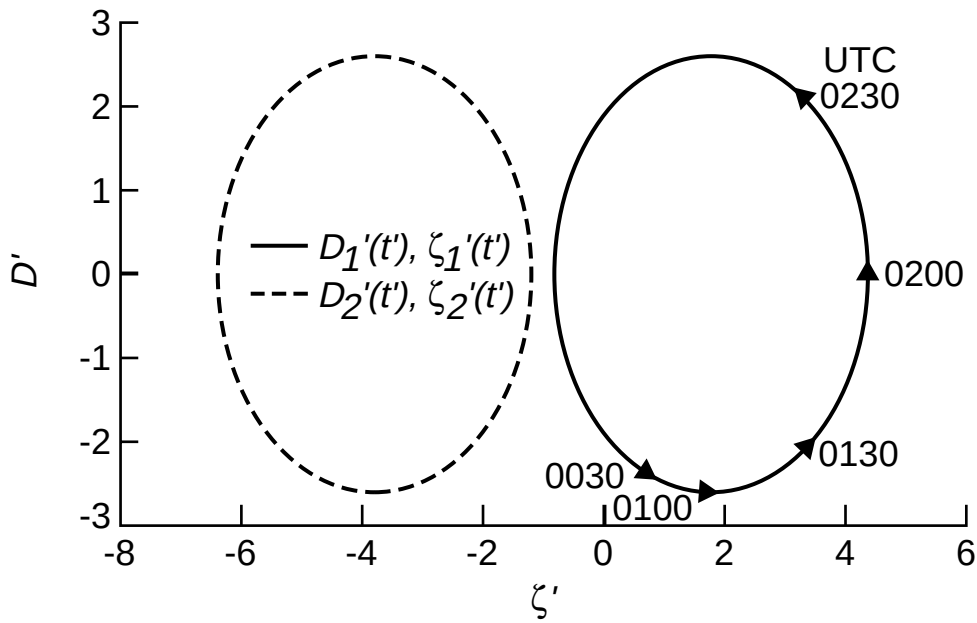

(a) Oscillations on the $\zeta' - D'$ phase plane.

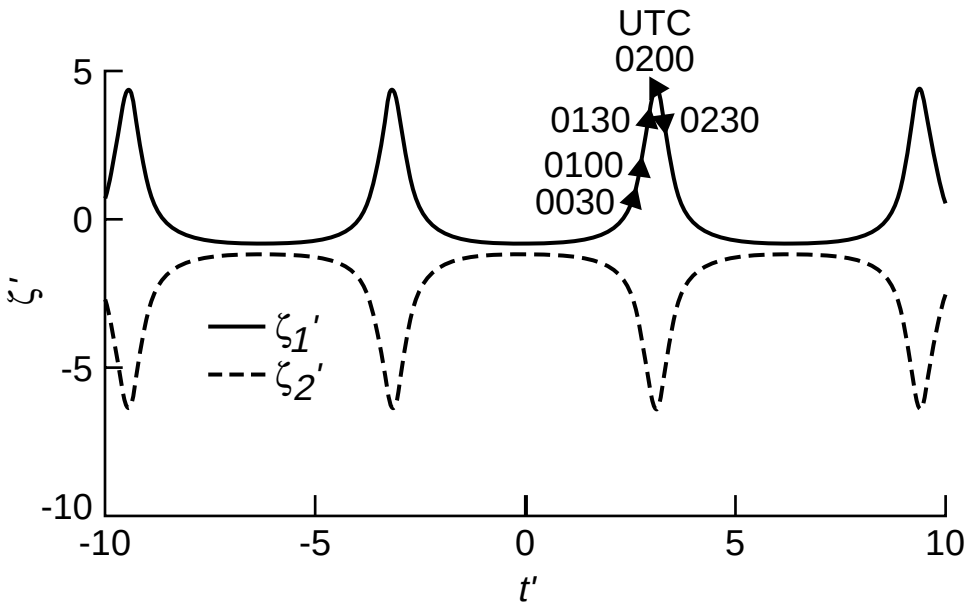

(b) Vertical vorticity ζ' versus t'.

Figure 2. PIO plots of solutions (33) and (32e) for $\zeta_{10}' = -0.814$ (Montana hailstorm simulation) and $\zeta_{20}' = -1.186$ with $D_0' = 0$. Primed quantities represent dimensionless core averages; solid triangles relate the simulation to universal time during the Montana hailstorm of 12 July 1981.

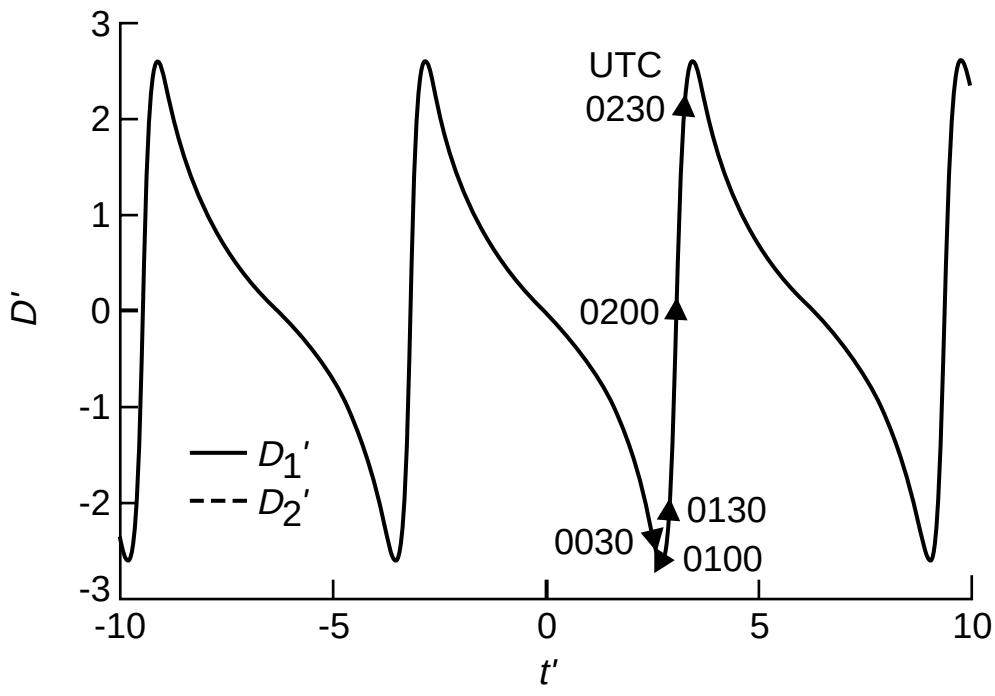

(c) Horizontal divergence D' versus t'.

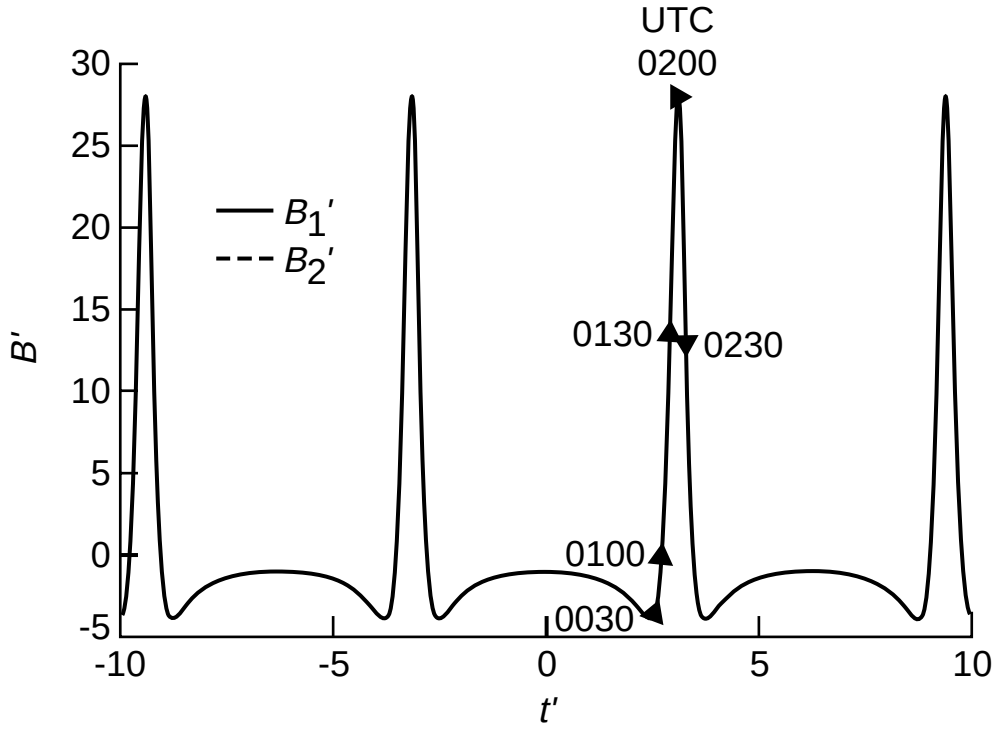

(d) Buoyancy B' versus t'.

Figure 2. Continued.

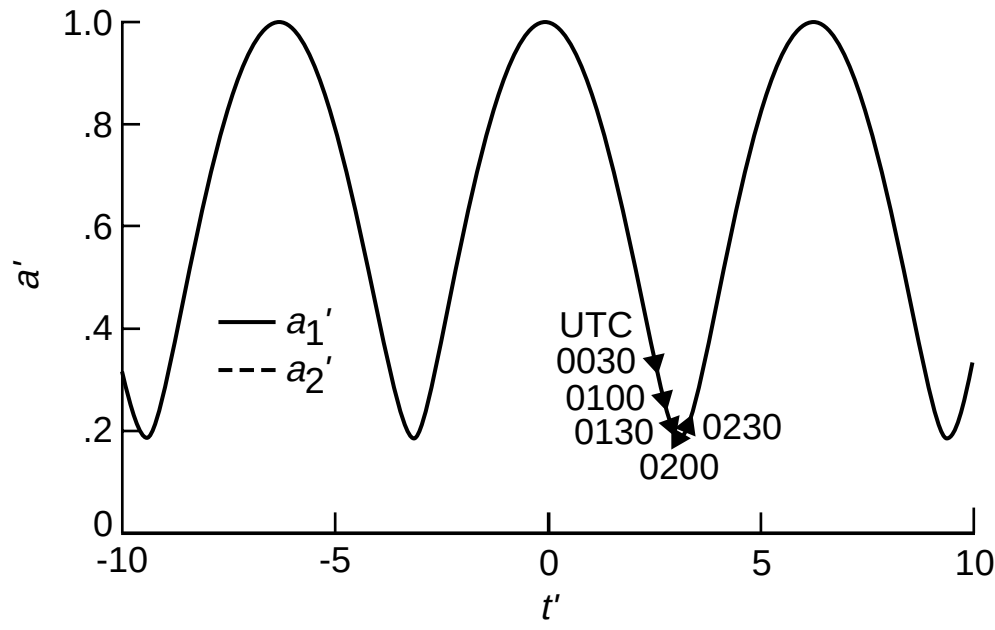

(e) Core radius a' versus t'.

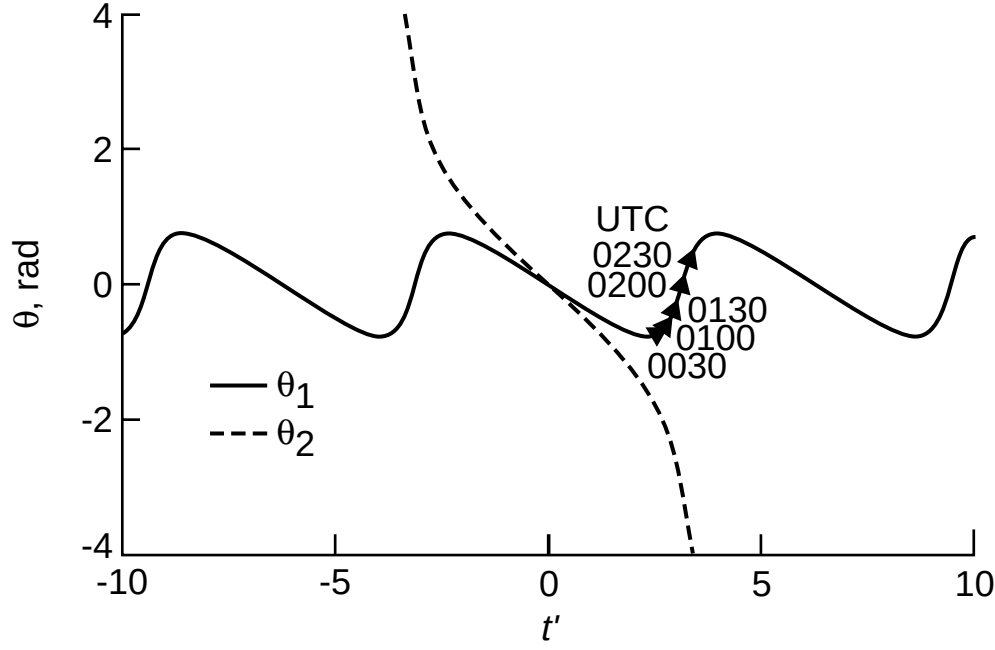

(f) Angular displacement of core fluid θ versus t'.

Figure 2. Concluded.

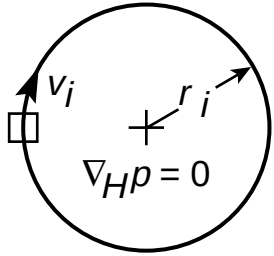

(a) Inertial oscillation of individual air parcel.

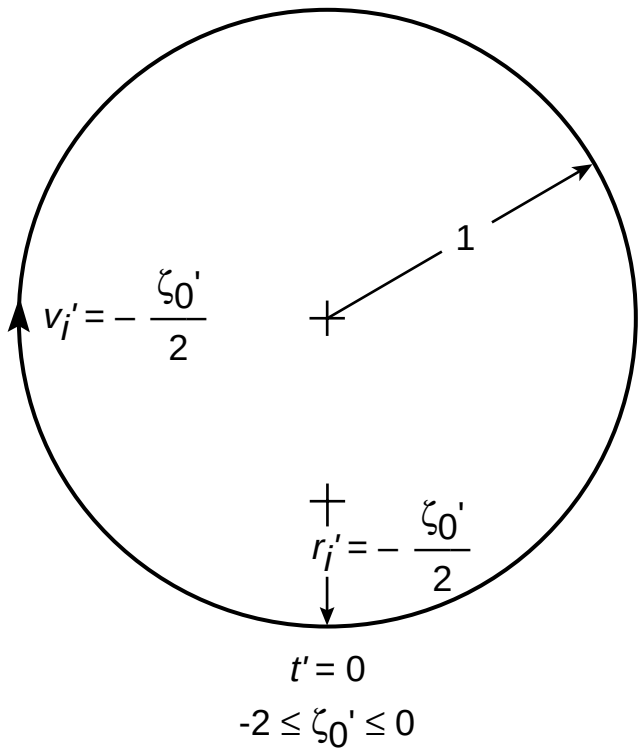

(b) Dimensionless model core at $t' = 0$ and inertial velocity v_i' and inertial radius r_i' of parcels on the periphery.

Figure 3. Aerial views showing physical nature of PIO oscillations in Figure 2.

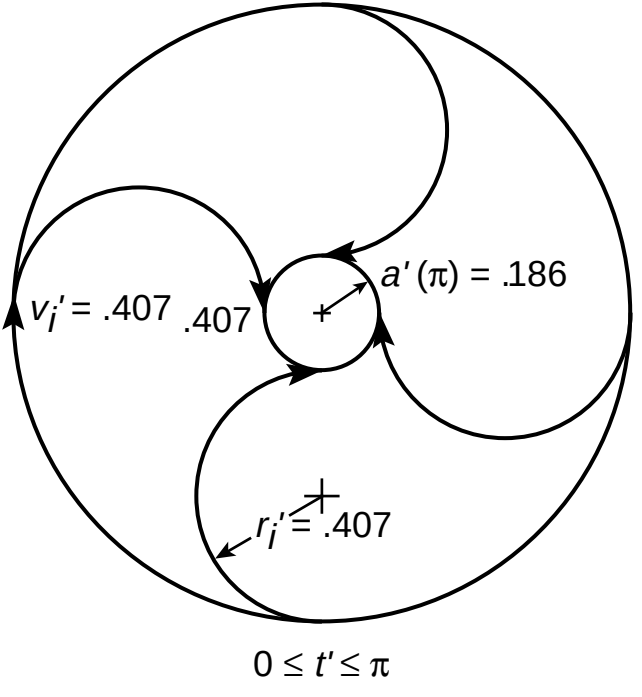

(c) Contraction and cyclonic spin-up for $\zeta_0' = -0.814$.

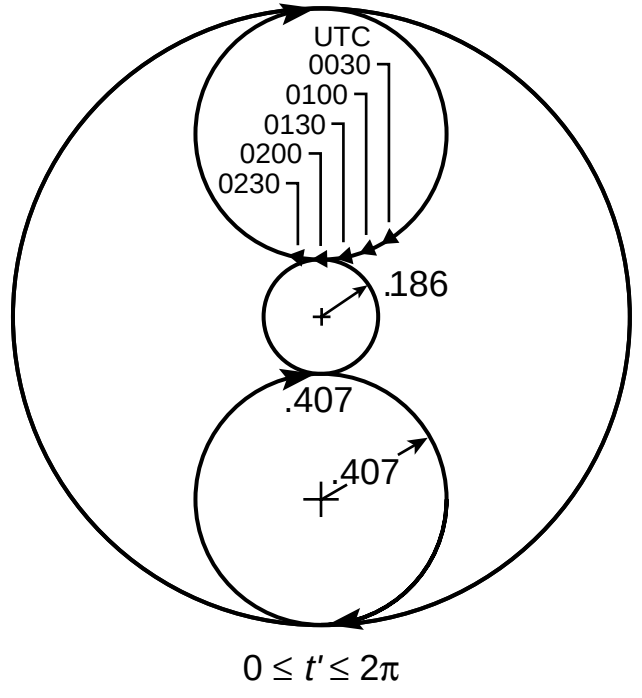

(d) Complete cycle for $\zeta_0' = -0.814$. Solid triangles are the same as in Figure 2.

Figure 3. Continued.

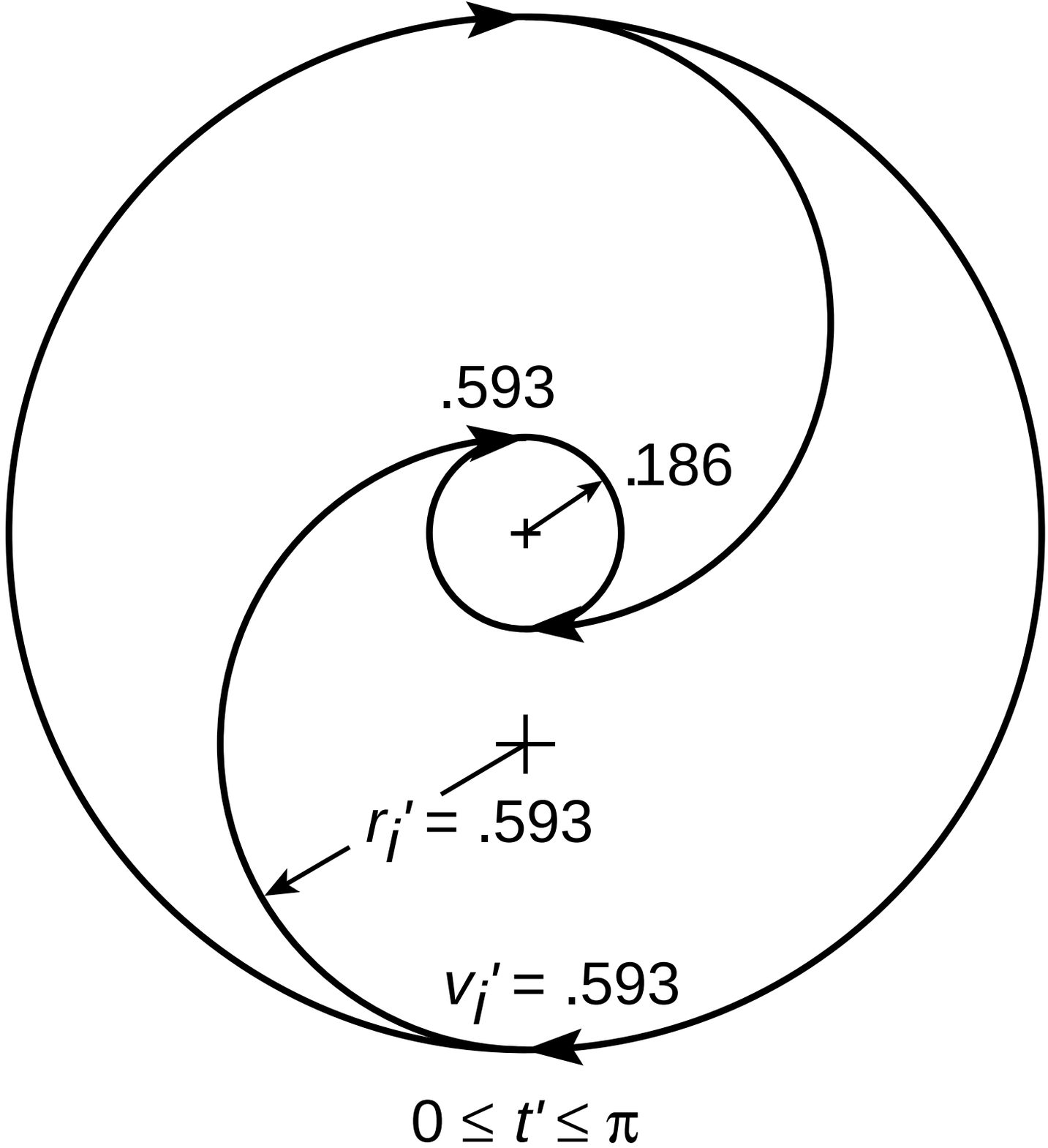

(e) Contraction and anticyclonic spin-up for $\zeta_0' = -1.186$.

Figure 3. Concluded.

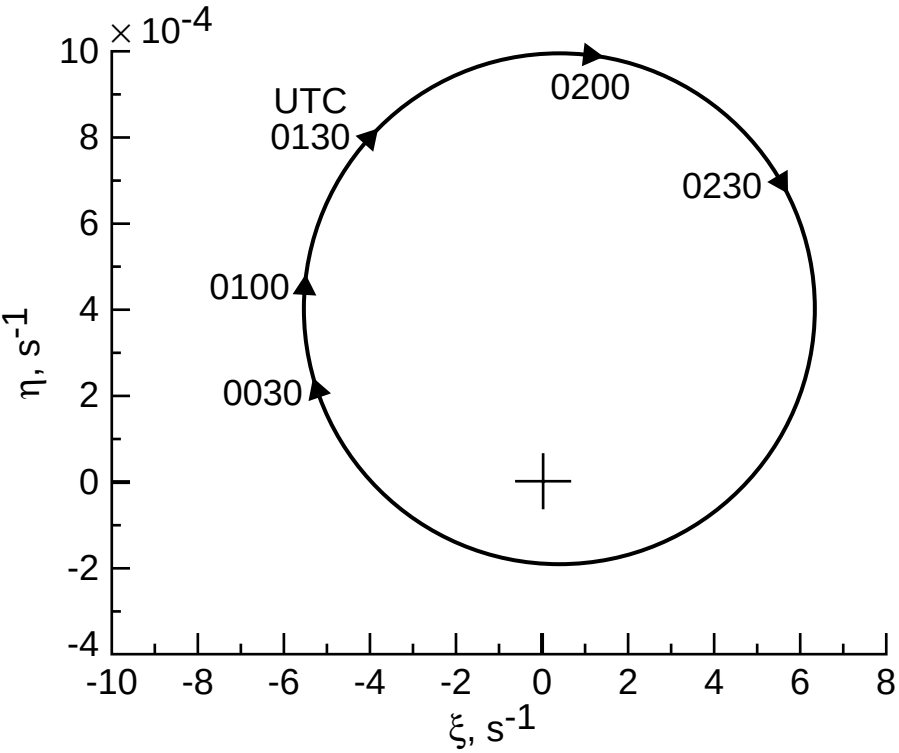

(a) Phase diagram of inner horizontal vorticity components ξ and η.

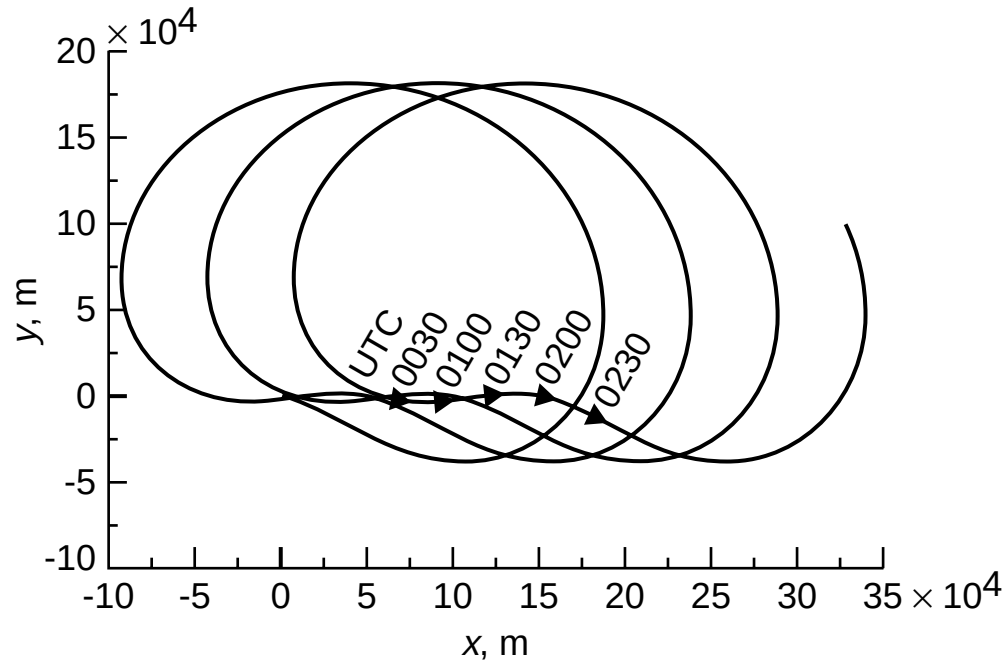

(b) Time track of model centerline on horizontal plane.

Figure 4. Numerical solutions of (9a), (9b), and (10) for the Montana hailstorm simulation. Initial values and parameters are listed in Table 1. Solid triangles are the same as in Figure 2.

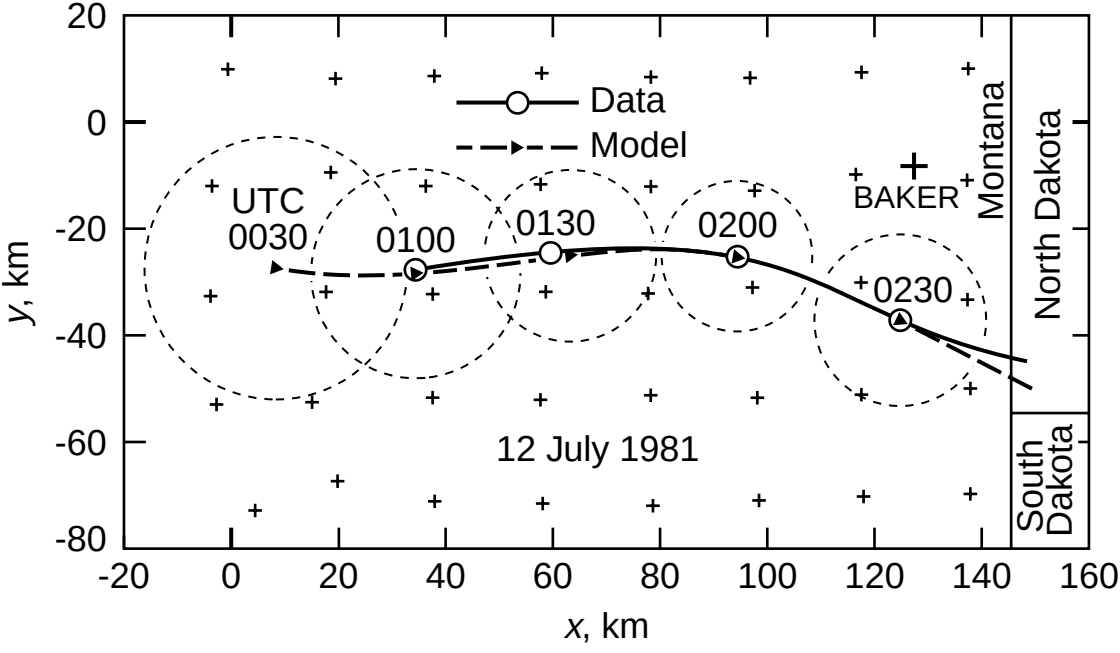

Figure 5. Theoretical and observed time tracks for Montana hailstorm on CCOPE mesonetwork. Data are from Fankhauser *et al*. [20]. Theoretical time track is from Figure 4(b), and theoretical core size is from Figure 2(e) and Table 1.

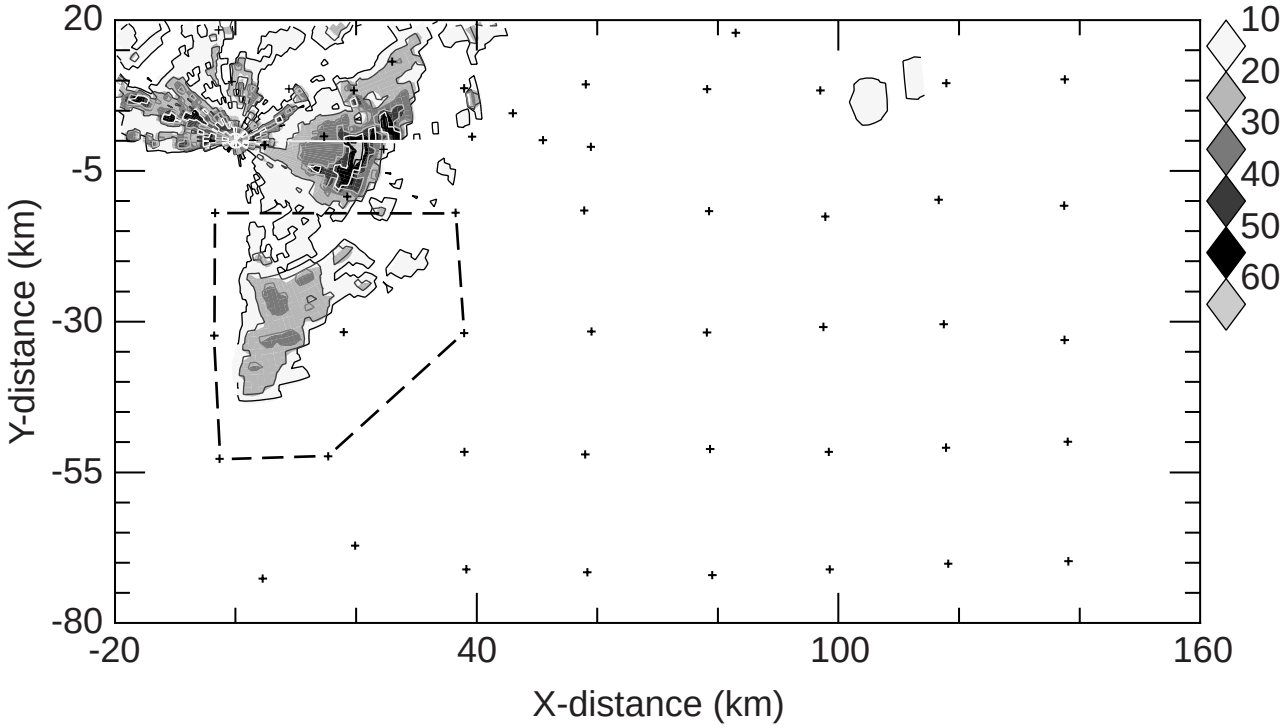

(a) 0030 (0030:36) UTC.

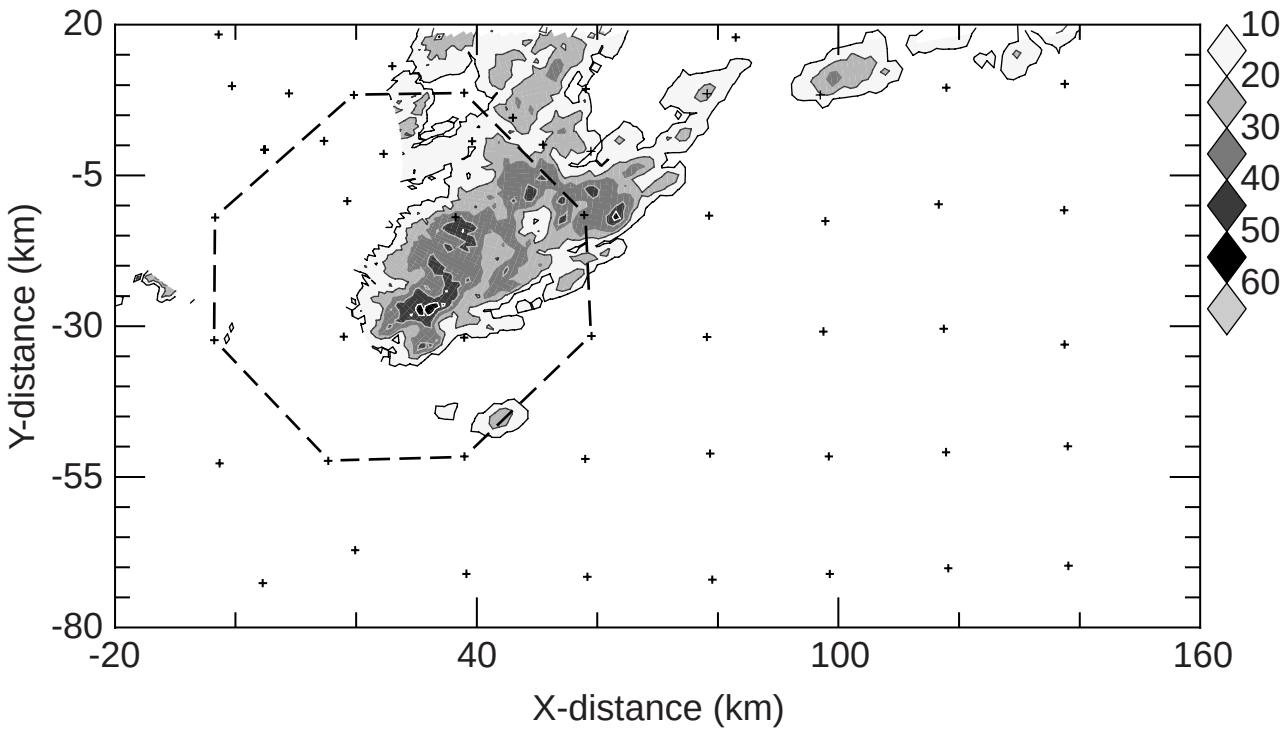

(b) 0100 (0102:05) UTC.

Figure 6. Low-level radar echoes from Montana hailstorm (12 July 1981) and corresponding surface analysis polygons superimposed on CCOPE mesonetwork. The reflectivity grayscale goes from 10 to 60 dBZ. Starting times of the radar scans are shown in parentheses.

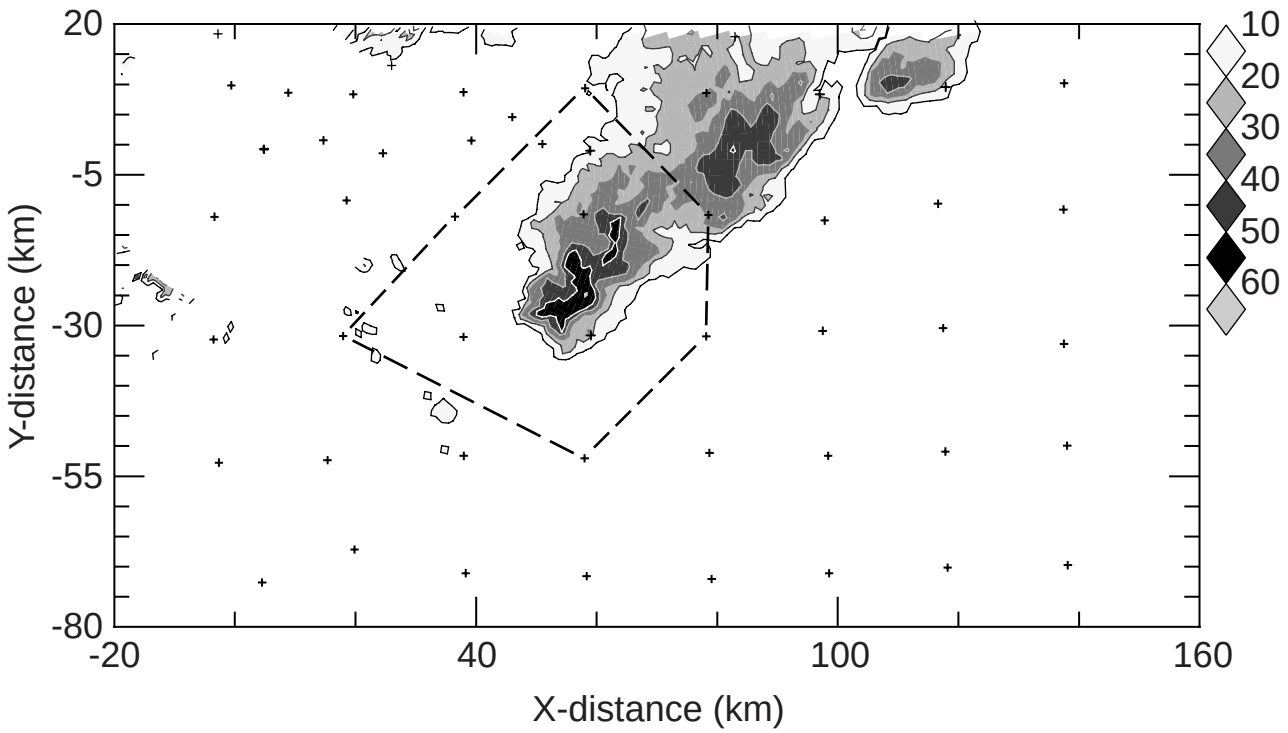

(c) 0130 (0132:05) UTC.

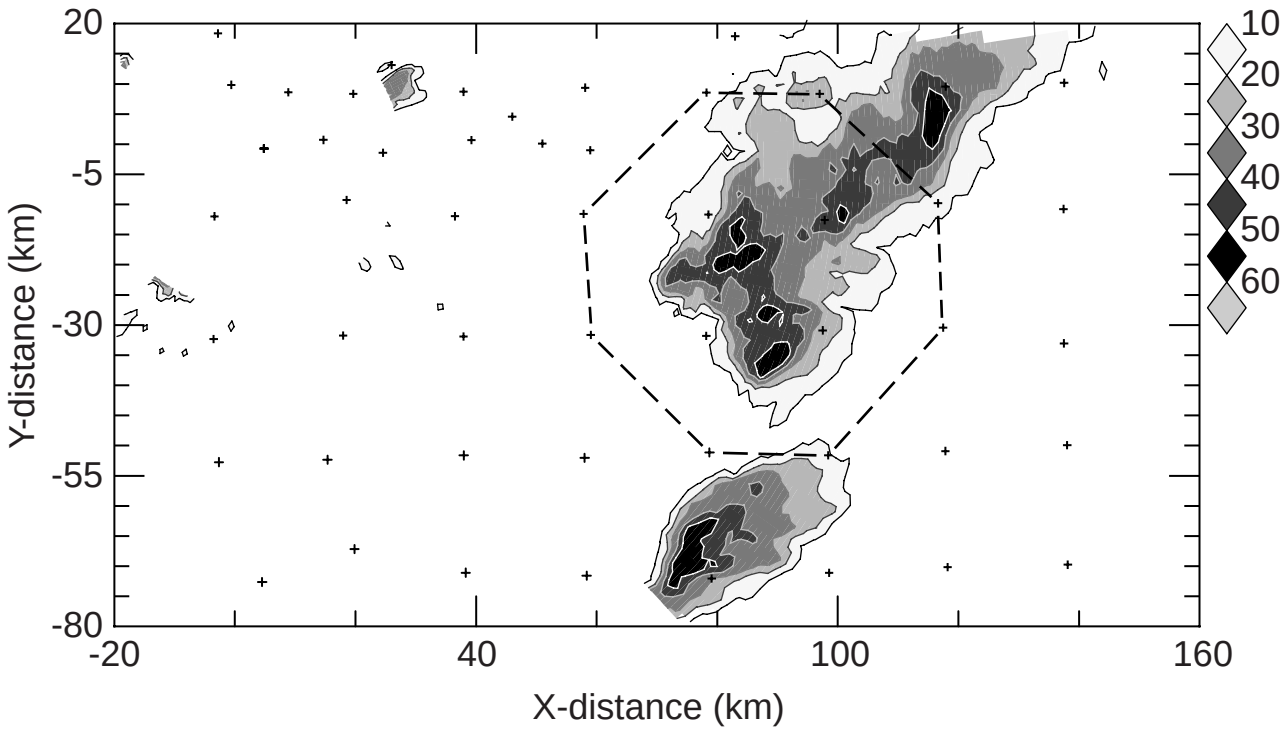

(d) 0200 (0202:19) UTC.

Figure 6. Continued.

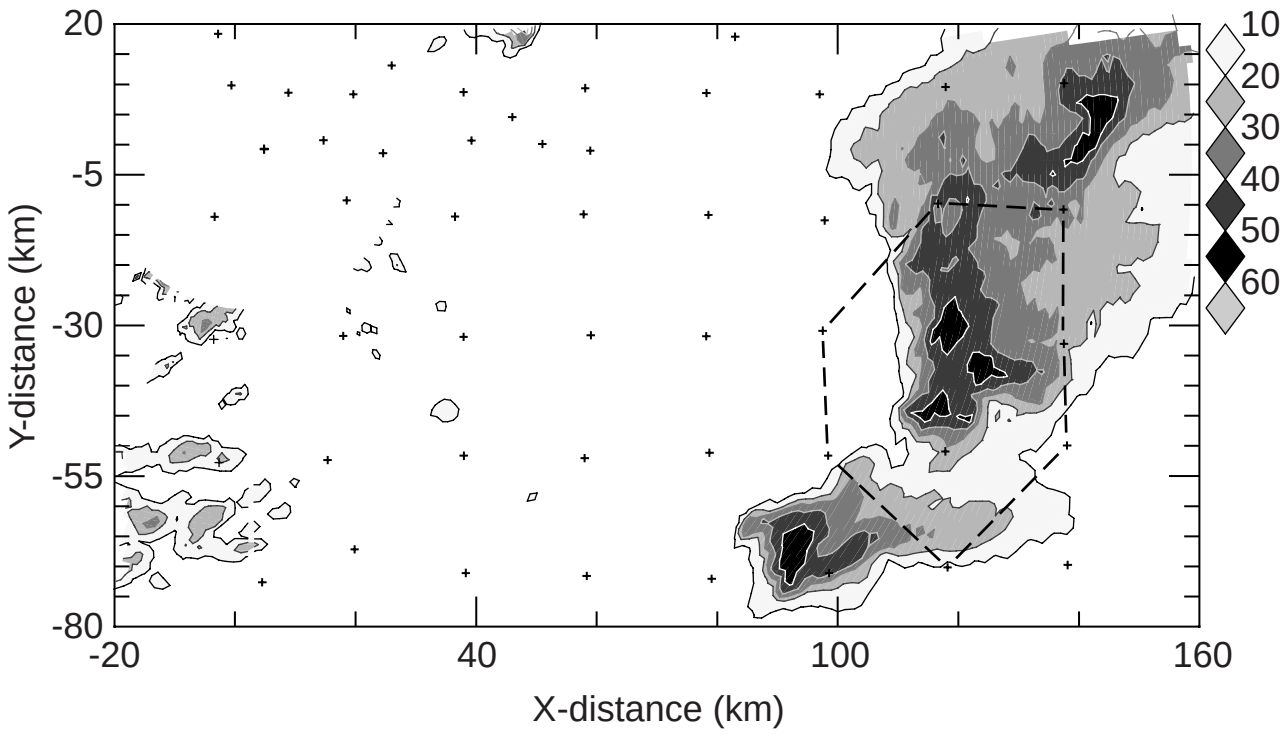

(e) 0230 (0232:14) UTC.

Figure 6. Concluded.

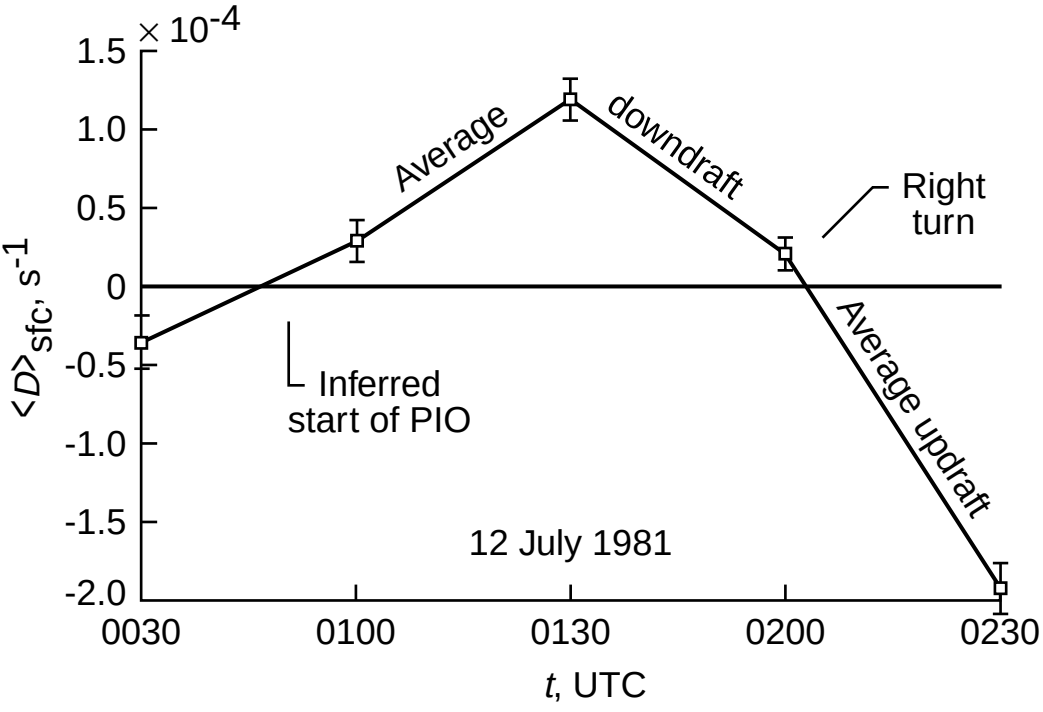

Figure 7. Average horizontal divergence $\langle D \rangle_{sfc}$ of winds measured near surface beneath Montana hailstorm versus t.

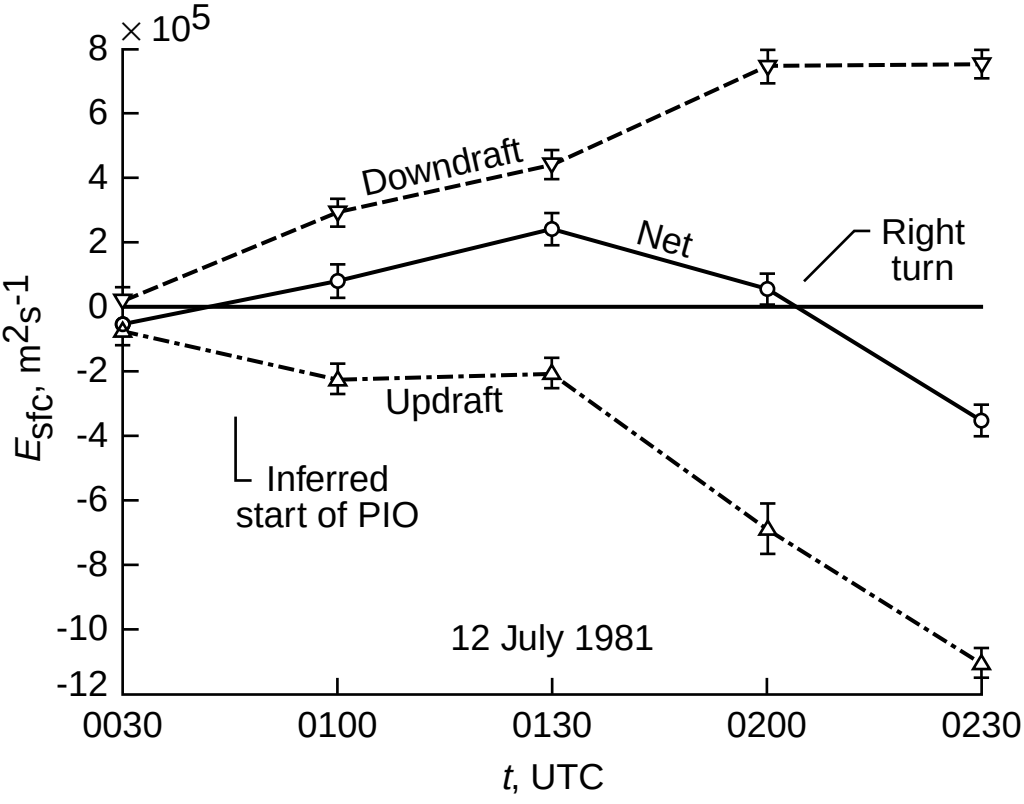

Figure 8. Updraft, downdraft, and net draft components of horizontal efflux E_{sfc} computed from winds measured near surface beneath Montana hailstorm versus t.